WARSAW UNIVERSITY OF TECHNOLOGY

ENGINEERING AND TECHNOLOGY

MATERIALS ENGINEERING

Ph.D. Thesis

Madhavi Dalsaniya, M.Sc.

Ab-initio modeling of reactivity of materials against fluorine under high pressure conditions

Supervisor

Prof. dr hab. inż. Krzysztof J. Kurzydłowski

Additional supervisor

dr hab. Dominik Kurzydłowski

WARSAW 2025

First, I would like to express my sincere gratitude to my supervisor, prof. dr. hab. inż. Krzysztof Jan Kurzydłowski for being humble, patient, and supportive at all times. His expert guidance and continuous encouragement have been deeply impactful to my progress.

I am also extremely thankful to my assistant supervisor, Dr. hab. Dominik Kurzydłowski for his insightful mentorship and unwavering support. His extensive knowledge and thoughtful guidance have shaped both my academic and personal growth. His dedication, generosity, and wisdom have been a continuous source of inspiration throughout my research and daily life. I feel truly privileged to have been part of his group, where I have learned so much from him. Words cannot fully express how grateful I am for his mentorship and kindness.

I extend my sincere thanks to Prof. Prafulla Kumar Jha (MSU, Vadodara, India) and Scientist Sanjeev Kane (RRCAT, Indore, India), who introduced me to this research-oriented path. Their unwavering belief in me and continuous encouragement, from my M.Sc. days onward, have been truly transformative. They taught me that no matter the circumstances, whether the days are good or bad you must keep moving forward. Their motivation has been a driving force and without their support, this journey would not have been possible.

A heartfelt thanks to my husband, Darshil, my unwavering pillar of strength. Thank you for patiently listening to me, keeping things light even in difficult moments, helping me stay calm, and always showing me the positive side of every situation. You remind me of my worth even when I doubt myself. Your belief in me, unconditional love, and support mean the world to me. Your virtual presence alone gives me confidence, assurance and peace of mind to keep going.

Finally, I am grateful to everyone who has supported and encouraged me throughout this *Ph.D. journey.*

Thank you all from the bottom of my heart!

This research was funded by,

National Science Centre (NCN), Poland, within the SONATA BIS Programme (grant number UMO-2019/34/E/ST4/00445).

Title: "J. BOND - Formation of new chemical bonds and superexchange pathways in fluorine rich-systems at high pressure".



SEED Scholarship under the NAWA STER-Internationalisation of Doctoral Schools Programme, Warsaw University of Technology (March 2022 to December 2023).



Research was carried out using computational resources provided by the Interdisciplinary Centre for Mathematical and Computational Modelling (ICM UW), the Poznań Supercomputing and Networking Center (PSNC). PLGrid provided access to the LUMI supercomputer through the EuroHPC Joint Undertaking and the LUMI consortium.





Abstract

High-pressure research provides fundamental insights into material properties, which are important in condensed matter theories, planetary science and materials engineering. Studies performed on molecular crystals such as H₂, O₂, N₂ and NH₃ have revealed remarkable phase transitions and exotic states of matter at pressures reaching hundreds of gigapascals, leading to unexpected bonding behaviors. These transformations, including metallization, polymerization and the formation of novel high-pressure phases, have helped us to better understand chemical and physical interactions in extreme environments.

In this aspect, halogens particularly bromine are used as a model system for studying pressure-induced molecular dissociation and electronic transitions. Iodine high-pressure phase transitions are extensively studied, while bromine behavior remains less explored, with unresolved questions regarding its phase stability, electronic properties, and intermediate phases. On the other hand, bromine fluorides introduce additional complexities in bonding and stability under compression, making them a subject of both fundamental and applied interest.

This thesis presents the results of computational studies on bromine and bromine fluorides under high-pressure conditions. In article A1, we confirm the phase transition sequence of bromine as follows: $Cmca \xrightarrow{90~GPa} Immm \xrightarrow{128~GPa} I4/mmm \xrightarrow{188~GPa} Fm\bar{3}m$. Our results show excellent agreement with experimental data, especially for the molecular Cmca phase. In article A2 we investigate the high-pressure behavior of bromine fluorides, confirming the stability of known compounds BrF3 and BrF5, and predicting two novel species, BrF2 and BrF6, as thermodynamically stable above 15 GPa. In article A3, we further explore the pressuredependent thermal and mechanical properties of bromine using density functional theory (DFT) combined with the quasi-harmonic approximation (QHA). These results reveal significant modifications in thermal expansion, heat capacity, and elastic stability with increasing pressure. Additionally, article A4 (currently unpublished) complements the theoretical results by presenting high-pressure X-ray diffraction experiments on bromine compressed up to 230 GPa and our simulations of the potential energy surface (PES) up to 180 GPa, further validating the predicted phase transition sequence. This research advances our understanding of molecular solids at high-pressure environments, laying the groundwork for future investigations in planetary science, condensed matter physics, and materials design.

Keywords: High pressure, molecular dissociation, phase transitions, halogens, density functional theory.

Streszczenie

Badania wysokociśnieniowe dostarczają podstawowych informacji na temat właściwości materiałów, ważnych w kontekście badań z zakresu fizyki ciał stałych, geologii i inżynierii materiałowej. Badania przeprowadzone na kryształach molekularnych, takich jak H₂, O₂, N₂ i NH₃, ujawniły niezwykłe przejścia fazowe i egzotyczne stany materii przy ciśnieniach sięgających setek gigapaskali, prowadzących do nieoczekiwanych zmian w wiązaniach chemicznych. Te przemiany, w tym metalizacja, polimeryzacja i tworzenie nowych faz wysokociśnieniowych, pomogły nam lepiej zrozumieć oddziaływania chemiczne i fizyczne w ekstremalnych warunkach.

W tym kontekście halogeny, w szczególności brom, służą jako układ modelowy do badania wywołanej ciśnieniem dysocjacji cząsteczkowej i przejść elektronowych. Podczas gdy przejścia fazowe jodu pod wysokim ciśnieniem są dobrze udokumentowane, zachowanie bromu pozostaje mniej zbadane, z nierozwiązanymi pytaniami dotyczącymi jego stabilności fazowej, właściwości elektronicznych i występujących faz pośrednich. Jednocześnie, fluorki bromu wprowadzają dodatkowe komplikacje w wiązaniu i stabilności pod ciśnieniem, co czyni je przedmiotem zarówno badań podstawowych, jak i aplikacyjnych.

Niniejsza rozprawa przedstawia wyniki badań numerycznych struktury i właściwości bromu i fluorków bromu w warunkach wysokiego ciśnienia. W artykule A1 potwierdzamy sekwencję przemian fazowych bromu: $Cmca \xrightarrow{90~GPa} Immm \xrightarrow{128~GPa} I4/mmm \xrightarrow{188~GPa} Fm\bar{3}m$. Uzyskane wyniki wykazują doskonałą zgodność z danymi eksperymentalnymi, zwłaszcza jeśli chodzi o strukturę i właściwości cząsteczkowej fazy Cmca. W artykule A2 opisano zachowanie fluorków bromu w warunkach wysokiego ciśnienia, potwierdzając stabilność znanych związków BrF₃ i BrF₅, a także przewidując, że dwa nowe związki, BrF₂ i BrF₆, są termodynamicznie stabilne powyżej 15 GPa. W artykule A3 przedstawiono kolejne wyniki dotyczące bromu, w tym zależne od ciśnienia właściwości termiczne i mechaniczne, wykorzystując teorię funkcjonału gęstości (ang. density functional theory, DFT) połączoną z przybliżeniem quasi-harmonicznym (ang. quasi-harmonic approximation, QHA). Wyniki te ujawniają znaczące zmiany rozszerzalności i pojemności cieplnej oraz stabilności mechanicznej zachodzące wraz ze wzrostem ciśnienia. Ponadto artykuł A4 (obecnie niepublikowany) uzupełnia wyniki teoretyczne, przedstawiając eksperymenty dyfrakcji rentgenowskiej bromu poddanego ciśnieniom sięgającym 230 GPa. Zawarto w nim także symulacje powierzchni energii potencjalnej (ang. potential energy Surface, PES) do 180 GPa, co dodatkowo potwierdza przewidywaną sekwencję przejść fazowych.

Zawarte w publikacjach wyniki wypełniają luki między badaniami eksperymentalnymi i teoretycznymi, oferując nowe spojrzenie na chemię halogenów w ekstremalnych warunkach. Badania te poszerzają wiedzę na temat kryształów cząsteczkowych w warunkach wysokiego ciśnienia, kładąc podwaliny pod przyszłe badania w zakresie nauk planetarnych, fizyki materii skondensowanej i projektowania materiałów.

Słowa kluczowe: Wysokie ciśnienie, dysocjacja cząsteczkowa, kryształy molekularne, przejścia fazowe, halogeny, teoria funkcjonału gęstości.

Table of Contents

1.	I	Introduction	15
	1.1	High-Pressure Science in Modern Research	16
	1.2	Molecular Crystals	17
	1.3	Reactivity of Fluorine	19
	1.4	Mechanical Properties	20
	1.5	Objectives, Hypothesis, and Scope of the Work	21
	1.6	Publications	22
	1.7	Conference Presentations and Summer Schools	23
2.	(Computational Methods and Formalisms	24
	2.1	The Schrödinger Equation	24
	2.2	Born-Oppenheimer Approximation	25
	2.3	Wavefunction-Based Approach	26
	2.3	3.1 Hartree Approximations	26
	2.3	3.2 Hartree-Fock Approximation	27
	2.4	Density Functional Theory	27
	2.4	4.1 Thomas-Fermi Theory	27
	2.4	4.2 Hohenberg-Kohn Theorems	28
	2.4	4.3 Kohn-Sham Approach	29
	2.5	Exchange-Correlation Functionals	30
	2.5	5.1 Local Density Approximation (LDA)	31
	2.5	5.2 Generalized Gradient Approximation (GGA)	31
	2.5	5.3 meta-GGA functionals (SCAN, r ² SCAN)	32
	2.5	5.4 Hybrid functionals (B3LYP, HSE06)	33
	2.6	Modelling Solid Materials with DFT	34
	2.6	6.1 Electron-Ion Interactions	34
	2.6	6.2 Plane Waves and Pseudopotential Method	34
	2.6	6.3 van der Waals Corrections	36
	2.6	6.4 LOBSTER: Bonding and Charge Analysis	38

	2.7	XtalOpt: An Open-Source Tool for Crystal Structure Prediction	39
	2.8	Phonon Structure	41
	2.9	Raman Spectroscopy	45
	2.10	Mechanical Properties	46
3.	S	ummary of Results	49
	3.1	High-Pressure Behavior of Solid Bromine	49
	3.2	Stability and Reactivity of Bromine Fluorides	52
	3.3	Thermal and Mechanical Behaviour of Bromine under High Pressure	54
	3.4	High-Pressure Behaviour of Solid Bromine - Experimental Validation	56
4.	C	onclusion and Future Work	59
Re	eferen	ices	60
Aŗ	pend	ix 1	72
Aŗ	pend	ix 2	87
Aŗ	pend	ix 3	102
Δτ	nend	iv 4	114

1. Introduction

"Pressure" is a fundamental thermodynamic variable that forces matter into a state very different from that observed in everyday conditions. While we typically experience only a small range of pressures, such as the atmosphere we breathe and the weight of the air pressing down on us, we rarely consider the extremes to which this invisible force can reach. The pressure range in the universe spans from 10⁻³² atm (in the emptiest part of the universe) to 10⁺³² atm (inside the core of a neutron star). Even within Earth's core, pressure can reach up to 3.6×10⁶ atm (360 GPa). Over billions of years, high pressures have played a crucial role in shaping planetary structures, driving chemical and geological transformations, and influencing the behaviour of materials deep inside stars and planets [1–4]. Because of its role in natural processes, high pressure also serves as both a probe and a tool in modern science and technology, altering atomic structures and electronic interactions to produce novel material properties [5,6].

It leads to transformative phenomena such as metallization [7], polymerization [8], superconductivity [9] and the emergence of novel chemical bonding arrangements [10]. These effects have opened the door for discoveries in materials science, including hydrogen-rich superconductors (H₃S [11], LaH₁₀ [12]), high-energy-density materials (cg-N) [8], superhard materials (c-BN) [13], and thermoelectric materials (PbTe) [14]. These breakthroughs have established high-pressure science as a cornerstone of modern materials science, influencing fields from condensed matter physics to energy storage and industrial applications.

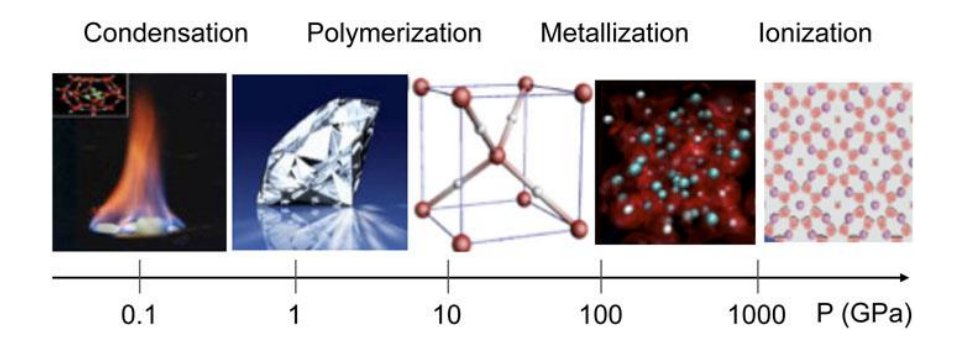


Fig. 1 Under extreme pressures, materials transform into novel states, such as methane hydrates (0.1 GPa), diamond (5 GPa), symmetric ice (80 GPa), metallic hydrogen (500 GPa), and Al electrides (10 TPa), adapted from ref. [5]

1.1 High-Pressure Science in Modern Research

The first high-pressure measurement technique (reaching ~10 GPa) was introduced by Percy W. Bridgman, who was awarded the Nobel Prize in 1946 for his contributions to high-pressure physics [15]. Since then, high-pressure research has evolved significantly, utilizing both static and dynamic compression methods. Static compression techniques, such as the one utilizing the diamond anvil cells (DACs) and large-volume presses (LVPs), are capable of applying continuous pressure. DACs are used to reach pressure in the multi-megabar range, whereas LVPs typically operate at about 50 GPa, making them ideal for studying systems in equilibrium. On the other hand, dynamic compression techniques, such as shock-wave and laser-driven approaches, generate much higher pressures (~5000 GPa) and temperatures (~1000 K) over microsecond timescales to investigate rapid phase transitions [5].

The effect of pressure on materials depends on how it is applied. Hydrostatic pressure is generated in contact with gas/liquid media and is uniform in all directions. Uniaxial compression in a constrained volume is applied along one axis, providing a simpler hydrostatic alternative. Quasi-hydrostatic stress refers to a state close to hydrostatic conditions but with small differences in principal stresses due to experimental limitations or medium properties, allowing for near-isotropic stress distribution with minimal deviatoric stress.

Recent in-situ measurement advancements, such as synchrotron X-ray diffraction [16] and Raman spectroscopy [17], have made it possible to directly observe electronic, vibrational, and structural changes in compressed materials [6,18]. Beyond fundamental research, high-pressure technology has transformed materials engineering by facilitating industrial processes such as high-pressure extrusion, hydroforming, and hot isostatic pressing, which enhance mechanical strength and electrical performance [19].

However, high-pressure experiments still face challenges such as limited sample volumes and/or short observation times, which can make direct measurements difficult. These difficulties led to close collaboration between theorists and experimentalists. Theoretical calculations of new compounds help identify potential targets for synthesis and provide insight into their structure and properties once experimental data become available. In this framework, density functional theory (DFT) offers a powerful computational approach, providing precise atomic-scale simulations of electronic structures, phase transitions, vibrational properties, magnetism and superconductivity under extreme pressures. Together, these complementary approaches have accelerated discoveries, pushing the boundaries of both fundamental research and real-world applications [20,21].

1.2 Molecular Crystals

Molecular crystals are a type of crystalline solid where molecules are arranged in a periodic structure and held together by intermolecular forces such as van der Waals, hydrogen bonding and $\pi - \pi$ interactions. These molecular crystals are widely studied in materials science, condensed matter physics, chemistry, and pharmaceuticals due to their tunable electronic, optical, mechanical, and thermal properties. Molecular crystals play a significant role in condensed matter physics enabling the study of quantum phenomena, charge transport mechanisms and phase transitions, thus contributing to the development of organic semiconductors [22] and superconductors [23] materials. When subjected to high pressure, molecular crystals undergo structural transformations due to the reduction in intermolecular distances, leading to phenomena such as metallization, or even molecular dissociation [24,25]. Their versatility in materials science allows for applications in smart materials, thermoelectric energy harvesting, and molecular actuators [26]. In pharmaceuticals, molecular crystals are important for drug formulation, as polymorphism directly impact drug solubility, stability, and bioavailability, which are important aspects in medicinal efficacy, as observed for example in aspirin and paracetamol [27]. By bridging fundamental physics, chemistry and engineering, molecular crystals continue to drive innovations in next-generation functional materials.

One of the most studied molecular systems is hydrogen (H₂), the simplest and lightest element in the periodic table. At extreme pressures above 350 GPa hydrogen is thought to transit into a metallic phase, where molecular bonds break and atoms rearrange into a dense atomic solid [28]. This transition is of particular interest as metallic hydrogen is predicted to be a room-temperature superconductor [7,24]. Despite the many theoretical and experimental studies devoted to this system, the exact nature of its transition to a metallic phase and its potential superconducting properties remain active areas of research [29–33]. Similarly, other diatomic molecules such as nitrogen (N₂), oxygen (O₂), and the halogens (F₂, Cl₂, Br₂, I₂) also undergo remarkable transformations under compression. Nitrogen is a naturally abundant element with a highly stable triple bond (N≡N). The molecular crystal of this element transforms into a polymeric structure with single N−N bonds at pressures above 110 GPa with temperature around 2000 K [34–36]. This polymeric phase of nitrogen is of great interest due to its potential as a high-energy-density material. In contrast, modelling indicates that oxygen requires much higher pressure (1920 GPa) to form a polymeric spiral chain structure [37–40].

Halogens are a group of extremely reactive nonmetallic elements in Group 17 of the periodic table, including fluorine (F), chlorine (Cl), bromine (Br), iodine (I) and astatine (At).

They are highly electronegative with fluorine being the most electronegative element in the Pauling scale. Halogen naturally exist as diatomic molecules (X_2) and readily react with metals to produce ionic salts (e.g., NaCl, KBr) featuring halide ions (X^-) . Due to their electron-rich nature, they participate in a wide range of chemical reactions and exhibit unique physical and electronic properties under extreme conditions.

Interestingly, halogens undergo pressure-induced metallization and dissociation like hydrogen. On the other hand, their electron-rich nature connects them to oxygen. However, polymerization occurs in halogens at much lower pressures as compared to hydrogen and oxygen. Among these elements, Br₂ and I₂ have been particularly interesting due to their relatively lower transition pressures making them more accessible for experimental and theoretical studies [41–45] as compared to F₂ and Cl₂ [46–48]. These elements undergo a series of phase transformations from molecular phase of *Cmca* symmetry through incommensurate structures exhibiting iodine chains to monoatomic phases displaying metallic properties. Iodine, which is a solid at ambient pressure and temperature, undergoes the following sequence of transitions $Cmca \xrightarrow{16\ GPa} Cmc2_1 \xrightarrow{20.8\ GPa} Fmmm(00\gamma)s00 \xrightarrow{32\ GPa} Immm \xrightarrow{43\ GPa} I4/mmm \xrightarrow{55\ GPa} Fm\overline{3}m$ [49,50].

Bromine is the only liquid halogen at ambient conditions. At room temperature it crystallizes into the molecular Cmca phase when compressed above 0.5 GPa [51]. As pressure increases, bromine follows a phase transition pathway similar to iodine. Several experimental [52–54] and theoretical [55–58] studies have been conducted on bromine, with ongoing research continuing to explore its high-pressure behaviour [50,59,60]. Despite these investigations, several unresolved questions remain regarding bromine's behaviour under extreme conditions. In particular, structural details and thermodynamic significance of incommensurate phase ($Fmmm(00\gamma)s00$) that emerges during the Cmca to Immm transition, are not fully resolved. A significant discrepancy also exists between experimentally determined phase boundary pressures of halogens and those predicted by density functional theory (DFT), raising concerns about the accuracy of current computational models. This concern stimulated part of our research undertaken in the framework of this thesis.

To bridge this gap and improve agreement between experimental and theoretical data, in our study we utilized the hybrid HSE06 functional to investigate the phase transition of solid bromine up to 200 GPa. The detailed results are presented in article A1 (see Appendix 1). These results enhance our understanding of bromine's high-pressure behaviour and contribute to a

broader comprehension of the fundamental principles governing molecular solids under extreme conditions.

1.3 Reactivity of Fluorine

Fluorine is the most electronegative halogen with an electronegativity of 4.0 in the Pauling scale. This high electronegativity introduces additional complexity due to strong oxidizing power and small atomic size [61]. Its high electron affinity allows it to attract electrons with great intensity, making it one of the most chemically reactive elements. Under ambient conditions, fluorine exists as diatomic molecules (F_2) , but due to its high reactivity, it rarely remains in molecular form when interacting with other substances at high pressure and temperature. Fluorine easily interacts with other elements to form fluorides, often stabilizing the element in its highest oxidation state. Well-known examples are sulfur hexafluoride (SF_6) as an electrical insulator, xenon hexafluoride (XeF_6) , and uranium hexafluoride (UF_6) for nuclear fuel processing. Additionally, fluorine-rich compounds offer greater mechanical strength which making them essential for wear-resistant coatings, as exemplified by polytetrafluoroethylene (PTFE). Furthermore, high-pressure fluorination can significantly enhance catalytic efficiency, particularly in energy-related technologies such as fuel cells.

Theoretical analysis based on DFT modelling, predict that under compression, fluorine should undergo significant structural and chemical transformations: a transition from the *Cmca* molecular phase to a monatomic tetragonal ($P4_2/mmc$) structure at 2500 GPa followed by a cubic phase ($Pm\overline{3}n$) at 3000 GPa [62]. These transformations attract interest of scientists because of its the theoretical and practical implications.

Calculations indicate that fluorine remains the most electronegative element under high pressure [63]. Its small atomic radius and high effective nuclear charge allow it to attract electrons more strongly than any other element. Most elements become more electropositive under pressure but fluorine electronegativity decreases slightly, allowing it to maintain its strong electron affinity [64]. This should lead to novel high-pressure phases with different bonding configurations, significantly impacting its molecular and electronic properties in extreme conditions.

One of the most intriguing aspects of fluorine chemistry is its reactivity with other halogens. Halogen fluorides (AF_x , where A = I, Br, Cl) represent an important class of compounds characterized by a wide range of coordination numbers (up to 8) and oxidation states (up to +7), making them valuable for exploring electron-rich bonding compound [65]. Both bromine

fluorides (BrF_x, x=1, 3, and 5), as well as iodine (IF_x, x=1, 3, and 5), and chlorine (ClF_x, x=1, 3, and 5) fluorides have been extensively studied in the gas phase [66–69] and in the solid state [70–73]. However, despite their importance, many aspects of their high-pressure phase transitions and bonding mechanisms remain unexplored.

To address these knowledge gaps in the theoretical description of halogen fluorides, we employed density functional theory (DFT) to model the high-pressure reactivity of bromine and fluorine up to 100 GPa. A comprehensive analysis of bromine fluorides behaviour under extreme conditions is provided in article A2 (see Appendix 2).

1.4 Mechanical Properties

Mechanical properties describe how materials respond to external applied forces that generate stresses. These properties, including elasticity, stiffness, hardness, ductility, and toughness are essential for understanding the structural integrity and performance of materials under varying conditions. In high-pressure research, mechanical properties play a crucial role in determining phase stability, deformation mechanisms, and structural transformations. The ability of a material to resist deformation or undergo phase transitions under pressure is often related by its elastic constants, bulk modulus, and shear modulus. These parameters help in predicting whether a material remains mechanically stable or transforms into a new structural phase.

Among the mechanical properties of solids, bulk modulus (B) is particularly significant, as it measures material's resistance to uniform pressure. A high bulk modulus indicates low compressibility and greater structural rigidity, while a low bulk modulus suggests that a material is more susceptible to pressure-induced volume reduction. For example, diamond (bulk modulus at ambient pressure, B₀, equal to 446 GPa) has the highest known bulk modulus, making it exceptionally resistant to compression, which is why it is commonly used in diamond anvil cell (DAC) experiments for generating extreme pressures. In contrast, crystals of noble gases like argon and helium have very low bulk moduli, making them highly compressible and useful as pressure-transmitting media in high-pressure studies.

The accuracy of mechanical property measurements at high pressures depends on maintaining hydrostatic conditions, where stress is applied uniformly in all directions. Under such conditions, elastic moduli such as bulk modulus and shear modulus can be precisely determined. However, at sufficiently high pressures all known pressure-transmitting media solidify, leading to non-hydrostatic stresses that may distort mechanical property

measurements [74]. To minimize these effects, soft pressure-transmitting media like argon, helium, and NaCl are commonly used in high-pressure experiments [75–77]. These media help ensure accurate assessment of elastic properties and phase transitions by reducing differential stress effects.

Elastic properties also play a critical role in phase stability and mechanical strength. At extreme pressures, materials often undergo increased hardness and reduced plasticity, leading to the formation of superhard phases such as cubic boron nitride (c-BN) and diamond-like carbon structures, which have applications in industrial coatings, high-strength tools, and advanced electronics. Furthermore, mechanical properties are correlated with electronic band structures and vibrational modes, which are key factors in understanding metallization, superconductivity, and high-pressure chemistry. To explore these effects, we conducted hybrid-DFT calculations to analyze the pressure-dependent thermal and mechanical behaviour of bromine up to 90 GPa. Further insights into the mechanical properties of bromine under high pressure are presented in article A3 (see Appendix 3).

1.5 Objectives, Hypothesis, and Scope of the Work

The primary **objective** of this study is to investigate the high-pressure behaviour of solid bromine (Br₂) and bromine fluorides (BrF_x) compounds with a particular focus on their structural phase transition, electronic, and mechanical properties, as well as reactivity under extreme conditions.

Specifically, this work **aims** to:

- Explain the high-pressure phase transitions of solid bromine (Br₂) up to 200 GPa, resolving discrepancies between experimental results and density functional theory (DFT) predictions.
- 2. Explore the reactivity of bromine and fluorine, and the possible formation of compounds (BrF_x) at high pressure, identifying new high-pressure phases, bonding mechanisms, and electronic transformations up to 100 GPa.
- 3. Analyse the mechanical properties and pressure dependent behaviour of bromine as a molecular crystal up to 90 GPa, focusing on bulk modulus, elastic moduli, and deformation behaviour through density functional theory (DFT) calculations used in conjunction with the quasi-harmonic approximation (QHA).

Through these objectives, this research aims to bridge the gap between theoretical predictions and experimental observations, leading to a more comprehensive understanding of halogen materials under extreme conditions.

We **hypothesize** that high-pressure phase transitions in bromine and bromine-fluoride compounds follow distinct pathways that differ from previous theoretical predictions. Specifically, we expect:

- 1. Solid bromine (Br₂) will undergo a series of phase transitions with pressure-dependent structural modifications up to 200 GPa, refining discrepancies between experimental observations and DFT calculations.
- 2. Bromine fluoride compounds (BrF_x) will exhibit unexpected bonding behaviour and electronic transformations under extreme pressures, potentially leading to new metastable phases.
- 3. Mechanical properties of bromine, including bulk modulus and mechanical stability, will follow a pressure-dependent trend, significantly influencing its elastic deformation under extreme conditions.

1.6 Publications

This research has resulted in three published journal articles (listed below), accumulating 100 and 140 ministerial points (MNiSW). These articles are included in Appendices 1-3 of this dissertation. An additional unpublished manuscript, currently in review in the journal *Physical Review B*, describes experimental validation of the phase transition in bromine, demonstrating an anharmonic, entropically driven approach to the close-packed metallic state. This work highlights how subtle enthalpy differences and lattice flexibility impact halogen behaviour under extreme conditions, offering new insight into high-pressure material physics. This work is included as Appendix 4.

- 1. <u>Madhavi H. Dalsaniya</u>, Krzysztof Jan Kurzydłowski, Dominik Kurzydłowski, <u>Insights into the high-pressure behaviour of solid bromine from hybrid DFT</u> <u>calculations.</u> Physical Review B, 106(11), 115128 (2022), IF = 3.2, MNiSW = 140. DOI: 10.1103/PhysRevB.106.115128
- 2. <u>Madhavi H. Dalsaniya</u>, Deepak Upadhyay, Krzysztof Jan Kurzydłowski, Dominik Kurzydłowski, *High-pressure stabilization of open-shell bromine fluorides*. Physical

- Chemistry Chemical Physics, 26(3), 1762-1769 (2024), IF= 3.6, MNiSW = 100. DOI: 10.1039/D3CP05020C
- 3. <u>Madhavi H. Dalsaniya</u>, Deepak Upadhyay, Paras Patel, Prafulla K Jha, Krzysztof Jan Kurzydłowski and Dominik Kurzydłowski, <u>Pressure-Dependent Thermal and Mechanical Behaviour of a Molecular Crystal of Bromine</u>. Molecules, 29(19), 4744 (2024), IF = 4.2, MNiSW = 140. DOI: 10.3390/molecules29194744
- 4. Eric Edmund, <u>Madhavi H. Dalsaniya</u>, Ross. T. Howie, E. Greenberg, Vitali Prakapenka, Miriam Peña-Alvarez, Michael Hanfland, Philip Dalladay-Simpson, Dominik Kurzydłowski and Andreas Hermann, <u>Close Packed Atomic Bromine up to 230 GPa</u>. (Physical Review B; Status: Under Review), (2025), IF = 3.2, MNiSW = 140.

1.7 Conference Presentations and Summer Schools

I have presented my research at three international conferences and two summer schools, both as oral and poster presentations:

- 1. **Oral presentation**: *Understanding the Chemistry and Bonding of Nitride and Polynitride Materials* at the 61st EHPRG Meeting that has taken place in Thessaloniki, Greece, at the Porto Palace Hotel (September 1-6, 2024).
- 2. **Poster presentation**: Exploring Solid Bromine and Bromine Fluorides Under High Pressure at the LOBSTER School 2024, Aalto University, Finland, (March 12-14, 2024).
- 3. **Oral presentation:** Theoretical investigation on the reactivity of fluorine and bromine at high pressure: emergence of novel bromine fluorides at the <u>Joint 28th AIRAPT and 60th EHPRG International Conference on High Pressure Science and Technology</u>, Edinburgh, UK (July 23-28, 2023).
- 4. **Summer School Participation:** Attended the <u>Scottish Universities Summer School in Physics 78 (SUSSP 78)</u> at the Centre for Science at Extreme Conditions an institute within the School of Physics and Astronomy at the University of Edinburgh, UK (July 18-23, 2023).
- 5. **Oral presentation:** *Insights into the high-pressure behaviour of solid bromine from hybrid DFT calculations* at the 59th European High Pressure Research Group Meeting (59th EHPRG) on High Pressure Science and Technology, Uppsala, Sweden, (September 5-8, 2022) received Best Oral Presentation Award.

2. Computational Methods and Formalisms

In the computational part of the thesis, we used *density functional theory (DFT)*, a quantum mechanical framework, to predict the ground-state properties of materials at the atomic scale. Computational tools such as *LOBSTER* for bonding analysis and *XtalOpt* an evolutionary algorithm for high-pressure structural prediction, were employed. Vibrational and elastic property calculations were performed using *Phonopy (version 2.18.0)*.

2.1 The Schrödinger Equation

Condensed matter systems are fundamentally described by quantum mechanics, where atomic interactions are dictated by Coulomb's law, which governs the electrostatic forces between charged particles. Quantum mechanics provides a robust framework for understanding simple systems, such as a single electron in a hydrogen atom, where the Schrödinger equation can be solved exactly to determine the quantum state [1]. However, the situation becomes significantly more complex for systems with multiple electrons. In such many-electron systems, the electrons interact not only with the positively charged nuclei but also with one another, leading to highly intricate correlation effects and exchange interactions. These complexities make the Schrödinger equation mathematically intractable for direct solutions. This raises the question of how can we study electron dynamics in atoms, molecules, and condensed matter systems which are many-electron systems. To address this, we start with the time-independent Schrödinger equation:

$$\widehat{H}\psi(r) = E\psi(r)$$
 (2.1)

where \widehat{H} is the Hamiltonian operator (containing the sum of the kinetic and potential energies), $\psi(r)$ is the wavefunction describing the quantum state of the electrons and ions and E is the total energy eigenvalue of the system. The Hamiltonian can be expressed as;

$$\widehat{H} = -\frac{\hbar^2}{2m} \nabla^2 + V(r) \quad (2.2)$$

In this Hamiltonian, the kinetic energy operator is represented by the $-\frac{\hbar^2}{2m}\nabla^2$ term, while V(r) term represent the potential energy of quantum system as a function of the position vector r.

In any physical system, where atoms are periodically arranged, the wavefunction depends on the coordinates of all particles in the system. This includes both the electrons and atomic nuclei positions: $\psi = f(r_1, r_2, \dots, r_N, R_1, R_2, \dots, R_N)$, as well as spin degrees of freedom. The many-body Hamiltonian for such systems includes contributions from the kinetic energy of electrons (\hat{T}_e) and ions (\hat{T}_n) , as well as potential energy terms for electron-electron $(\hat{V}_{e,e})$, electron-ion $(\hat{V}_{e,n})$ and ion-ion $\hat{V}_{n,n}$ interactions [79]:

$$\hat{H} = \hat{T}_e + \hat{T}_n + \hat{V}_{e,e} + \hat{V}_{e,n} + \hat{V}_{n,n}$$
 (2.3)

This leads to the full time-independent Schrödinger equation:

$$\widehat{H}\psi(r) = \left\{ -\frac{\hbar^{2}}{2m_{e}} \sum_{l} \frac{\partial^{2}}{\partial r_{i}^{2}} - \frac{\hbar^{2}}{2M_{l}} \sum_{l} \frac{\partial^{2}}{\partial R_{l}^{2}} + \frac{1}{2} \sum_{\substack{l,l'\\l \neq l'}} \frac{e^{2}}{4\pi\varepsilon_{0}} \frac{Z_{l}Z_{l'}}{|R_{l} - R_{l'}|} + \frac{1}{2} \sum_{\substack{i,j\\i \neq j}} \frac{e^{2}}{4\pi\varepsilon_{0}} \frac{1}{|r_{i} - r_{j}|} - \sum_{l} \sum_{\substack{l}l} \frac{e^{2}}{4\pi\varepsilon_{0}} \frac{Z_{l}}{|r_{l} - R_{l'}|} \right\} \psi(r) = E\psi(r) \quad (2.4)$$

In this equation, \hbar is the reduce Planck's constant, m_e and M_l are masses of electrons and ions, Z is the charge of ion, e is the charge of electron and r, R denote the positions of electrons and ions. The terms $|R_l - R_{l'}|$, $|r_l - r_j|$ and $|r_l - R_{l'}|$ represent the distances between ions, electron, and that between electrons and ions, respectively. Solving this equation reveals the ground-state energy of the system. From this, the ground-state properties of the material under equilibrium conditions can be determined. Due to the equation's complexity, especially in large systems, it's hard to solve. Therefore, several approximations to this theory were proposed which are discussed in detail in the proceeding sections.

2.2 Born-Oppenheimer Approximation

The first major approximation, introduced by Max Born and J. Robert Oppenheimer in 1927 [80], simplifies the many-body Schrödinger equation by separating electronic and nuclear motion. It is based on the fact that the ratio of ion mass to electron mass is approximately 10⁴, meaning ions move significantly slower than electrons. This allows electrons to be treated independently, assuming static ions. Under this approximation, the kinetic energy of the ion term is negligible, and the ion-ion potential becomes a constant. The modified equation (2.3) is written as:

$$\widehat{H} = \widehat{T}_e + \widehat{V}_{e,e} + \widehat{V}_{e,n} + Constant$$
 (2.5)

Grouping nuclear contributions into an external potential simplifies the Hamiltonian further:

$$\widehat{H} = \widehat{T}_e + \widehat{V}_{e,e} + \widehat{V}_{ext} \quad (2.6)$$

$$\widehat{H}\psi(r) = \left\{ -\frac{\hbar^2}{2m_e} \sum_{l} \frac{\partial^2}{\partial r_l^2} + \frac{1}{2} \sum_{\substack{i,j \ i \neq j}} \frac{e^2}{4\pi\varepsilon_0} \frac{1}{|r_i - r_j|} - \sum_{l} \sum_{l} \frac{e^2}{4\pi\varepsilon_0} \frac{Z_l}{|r_i - R_{l'}|} \right\} \quad (2.7)$$

This approximation significantly simplifies the many-body Schrödinger equation by focusing on electronic motion while treating ion as static. However, in most cases this approximation is still insufficient to solve the Schrödinger equation and therefore more approximations are needed which leads us to Hartree and Hartree-Fock approaches.

2.3 Wavefunction-Based Approach

2.3.1 Hartree Approximations

The Hartree approximation further simplifies the many-electron Schrödinger equation by treating electrons as independent particles moving in an average field [81–84]. The many-electron wavefunction is approximated as a product of single-particle wavefunctions:

$$\psi(r_1, r_2, \dots, r_N) \approx \psi_1(r_1)\psi_2(r_2)\dots\psi_N(r_N)$$
 (2.8)

This leads to a single-electron equation:

$$\left(-\frac{\hbar^2}{2m_e}\sum_i \frac{\partial^2}{\partial r_i^2} + \hat{V}_{ext} + \hat{V}_H\right)\psi_i(r) = E_i\psi_i(r) \quad (2.9)$$

here, the Hartree potential \hat{V}_H is defined as:

$$\hat{V}_H = \int \frac{\rho(r')}{|r-r'|} d^3r'$$
 (2.10)

here $\rho(r')$ represent the electron density and is given by:

$$\rho(r') = \sum_{i} |\psi_{i}(r')|^{2} (2.11)$$

where $\psi_i(r')$ are the single-electron wavefunctions. While this method uses a mean-field approximation, it does not account for electron correlations or the Pauli exclusion principle. Consequently, this method also neglects exchange interactions, necessitating additional refinements for more accurate descriptions [85,86].

2.3.2 Hartree-Fock Approximation

The Hartree-Fock method improves upon Hartree by incorporating the Pauli exclusion principle and exchange interactions through antisymmetric wavefunctions [87,88]:

$$\psi(r_{1}, r_{2}, ..., r_{N}) = \frac{1}{\sqrt{N!}} \begin{vmatrix} \psi_{1}(r_{1}) & \psi_{2}(r_{1}) & ... & \psi_{N}(r_{1}) \\ \psi_{1}(r_{2}) & \psi_{2}(r_{2}) & ... & \psi_{N}(r_{2}) \\ \vdots & \vdots & \ddots & \vdots \\ \psi_{1}(r_{N}) & \psi_{2}(r_{N}) & ... & \psi_{N}(r_{N}) \end{vmatrix}$$
(2.12)

The normalization factor $\frac{1}{\sqrt{N!}}$ ensures that the wavefunction maintains its statistical validity. By minimizing the total energy using the Lagrange multiplier method, the Hartree-Fock equations are derived:

$$\left(-\frac{\hbar^{2}}{2m_{e}}\sum_{i}\frac{\partial^{2}}{\partial r_{i}^{2}}+\hat{V}_{ext}+\hat{V}_{H}\right)\psi_{i}(r)-\sum_{j}\int\frac{\psi_{j}^{*}(r')\,\psi_{i}(r')}{|r-r'|}d^{3}r'\psi_{j}(r)=E_{i}\psi_{i}(r) \quad (2.13)$$

Hartree-Fock accounts for exchange interactions but ignores Coulomb electronic correlation, meaning it does not fully capture electron-electron interactions beyond the mean-field approximation. This leads to inaccuracies in computed energies, especially for strongly correlated systems. Density functional theory (DFT) addresses these challenges by reformulating the many-body problem in terms of the electronic density rather than wavefunctions. This makes it computationally more efficient while approximating both exchange and correlation effects through functionals.

2.4 Density Functional Theory

Hohenberg and Kohn introduced new theory in 1964, for solving many-electron systems through the electron density $n(\vec{r})$, which depends only on 3 spatial coordinates. This theory is known as density functional theory (DFT). This was a breakthrough in the field due to its cost effectiveness as many electron systems could be reduced to single electron density. The Thomas-Fermi theory, Hohenberg-Kohn theorems and Kohn-Sham equations, constitute the basic framework of DFT. All these theories will be discussed in next subsections.

2.4.1 Thomas-Fermi Theory

Before the Hohenberg and Kohn theorems, Thomas and Fermi introduced in 1927 the first ever theory based on electron density (*i.e.* the function describing the probability of finding an

electron in an infinitesimally small spatial region) [89,90]. The theory introduced electron density instead of single particle wave function as a basic variable. In the case of N interacting electrons, the kinetic energy in terms of electron density $n(\vec{r})$ is given by:

$$T_{TF} = C_k \int n(\vec{r})^{\frac{5}{3}} d^3r$$
 (2.14)

Where the constant C_k is

$$C_k = \frac{3}{10} (3\pi^2)^{2/3} \frac{\hbar^2}{2m}$$

Now, the total energy can be written as a functional of $n(\vec{r})$ in form of the summation of kinetic energy, external potential (V_{IE}) and electrostatic energy, which is,

$$E = T_{TF} + \int V_{IE}(\vec{r}) n(\vec{r}) d^3r + \frac{1}{2} \iint \frac{e^2}{4\pi\varepsilon_0} \frac{n(\vec{r}') n(\vec{r})}{|\vec{r} - \vec{r}'|} d^3r d^3\vec{r}' \quad (2.15)$$

Thomas-Fermi theory was the groundwork of the DFT; however, the semi-classical expression of the energy was its drawback.

2.4.2 Hohenberg-Kohn Theorems

The density-based approach then further elaborated by the Pierre Hohenberg and Walter Kohn in terms of two theorems which serve as the theoretical core of the DFT [91]. The theorems are as follows:

Theorem I: Existence and Uniqueness: the ground-state electron density $n(\vec{r})$ uniquely determines the external potential $\hat{V}_{ext}(\vec{r})$ acting on the system. The exact statement is the: "The external potential $\hat{V}_{ext}(\vec{r})$ is a unique functional of the electron density $n(\vec{r})$. As a result, the total ground state energy E of any many body systems is also a unique functional of $n(\vec{r})$, that is, E = E[n]."

Theorem II: Variational Principle: the system's ground-state energy is achieved at the lowest value of the energy functional, which occurs exclusively when the input density is equal to the ground-state density $n(\vec{r})$. The statement is as follows: "The functional E[n] for the total energy has a minimum equal to the ground-state energy at the ground-state density."

The theorem provides a foundation for a variational strategy, allowing the optimization of an initial density to the true density using a self-consistent approach, as implemented in various DFT software tools.

2.4.3 Kohn-Sham Approach

Using Hohenberg-Kohn theorems, Kohn and Sham (KS) came up with a better approach where they replace N-electrons with fictious system of one electron [92,93]. In the KS method, a single-particle potential $V_{eff}(r)$ is defined, which generates the same ground-state electron density as the interacting system. As a result, the total energy is formulated within this framework as follows:

$$E_{KS}[n] = T_S[n] + E_H[n] + E_{xc}[n] + \int V_{ext}(\vec{r}) n(\vec{r}) d^3r$$
 (2.16)

where $T_S[n]$ is non-interacting kinetic energy and $E_H[n]$ is energy term under Hartree approximation. The $T_S[n]$ and $E_H[n]$ can be defined as,

$$E_{H}[n] = \frac{1}{2} \iint \frac{n(\vec{r}') n(\vec{r})}{|\vec{r} - \vec{r}'|} d^{3}r d^{3}\vec{r}' \quad (2.17)$$

$$T_{S}[n] = -\frac{1}{2} \sum_{i}^{N} \langle \phi_{i} | \nabla^{2} | \phi_{i} \rangle \quad (2.18)$$

$$n(r) = \sum_{i}^{N} |\phi_{i}(r)|^{2} \quad (2.19)$$

$$N = \int n(\vec{r}) d^{3}r \quad (2.20)$$

Here, $T_S[n]$ was described in the context of KS orbitals. The term E_{xc} is a summation of two energies, namely exchange energy E_x and correlation energy E_c . The exchange energy is consequence of the anti-symmetric characteristics of the wave function as it changes the under the position exchange. The correlation energy is due to the repulsive force between the two electrons in the orbit. The term that puts DFT above HF is V_{xc} , which is the functional derivative of the E_{xc} . However, the exact form of exchange correlation functional is unknown. The term V_{xc} can be written as;

$$V_{xc}[n(r)] = \frac{\delta E_{xc}[n(\vec{r})]}{\delta n(\vec{r})} \quad (2.21)$$

The motion of electrons occurs within an effective potential V_{eff} , which indirectly includes the effects of electronic interactions. The electron-electron interactions in the KS equations are

replaced by a coupling between electrons and an effective medium. The KS equation in the Schrödinger form is written as;

$$\widehat{H}_{KS}\phi_i(r) = E_{KS}\phi_i(r) \quad (2.22)$$

and the Hamiltonian is;

$$\widehat{H}_{KS} = -\frac{1}{2} \sum \nabla^2 + V_{eff}$$
 (2.23)

In Hamiltonian, the sum of the three potentials $(V_{ext} + V_H + V_{xc})$ is included as the V_{eff} term. By iteratively adjusting the non-interacting electron density to match the ground state density of the real interacting system, the self-consistent method is used to solve the Hamiltonian. Starting with an initial density guess, the potential terms are recalculated until the energy stabilizes at a convergent value. By transforming the many-electron problem into a one-electron problem, the KS approach achieves significant efficiency. Despite its effectiveness, the true form of the exchange-correlation functional (V_{xc}) cannot yet be determined precisely, requiring approximations that are addressed in the subsequent section.

2.5 Exchange-Correlation Functionals

To determine the accurate results using KS approach one needs to identify the true exchange-correlation functional. Over the time, many theories have been explored to predict the correct results. The idea of Jacob's ladder [94] helps organize and interpret these techniques

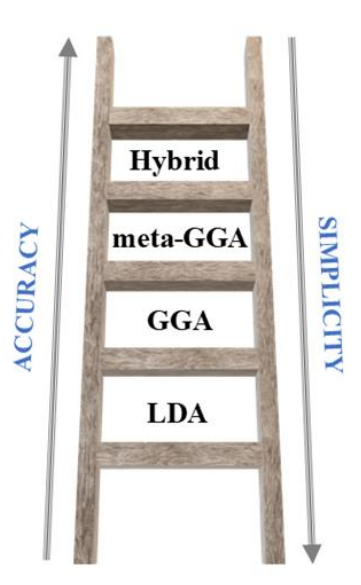


Fig. 2 The "Jacob's ladder" of density functional approximations. Higher levels mean greater accuracy and cost.

highlighting how aiming for higher accuracy (moving to higher rungs of the ladder) leads to greater computational requirements for the analyzed system. The exchange-correlation can be classified in the three different categories based on the degree of information they incorporate about the electron density: local, semi-local and non-local functionals. The local functional involve local density approximation (LDA), semi-local functionals involving generalized gradient approximation (GGA) and meta-GGA, while non-local involves hybrid functionals.

2.5.1 Local Density Approximation (LDA)

The LDA, developed by Kohn and Sham, is a fundamental method for approximating E_{xc} . This approach assumes that the electron density varies so slowly that it can be considered uniform within small spatial regions [95]. In this regard, an effective way to approximate the electron density involves modeling it locally as a homogeneous electron gas. The E_{xc} is then computed by integrating energy density over the entire spatial domain of this gas. The E_{xc} for LDA can be written as;

$$E_{xc}^{LDA}[n(\vec{r})] = \int n(\vec{r}) \, \epsilon_{xc}[n(\vec{r})] d^3r \quad (2.24)$$

where ϵ_{xc} is exchange-correlation energy per particle for electron gas with density $n(\vec{r})$ [94]. The LDA excels in modeling the physical properties of metals and systems analogous to a homogeneous electron gas. This capability likely stems from the localized nature of exchange-correlation interactions in such materials. Despite its versatility across many material types, LDA falters when confronted with systems exhibiting non-uniform electron density or significant electron correlation effects. Notable failures include the underestimation of band gaps in semiconductors and insulators and inaccuracies in determining lattice constants and bond lengths in weakly bonded molecular systems [96].

2.5.2 Generalized Gradient Approximation (GGA)

We know that real systems inherently lack perfect homogeneity and exhibit varying density distributions surrounding electrons. Recognizing this, Herman in 1969 proposed the foundation for the GGA. This method enhances the accuracy of exchange-correlation functionals by considering both the electron density and its gradient, combining local and semi-local aspects [97]. The GGA approximated E_{xc} can be given as;

$$E_{xc}^{GGA}[n(\vec{r})] = \int n(\vec{r}) \, \epsilon_{xc}[n(r), \nabla [n(\vec{r})]] d^3r \quad (2.25)$$

The more accurate results as compared to LDA stems from inclusion of non-local effects in the exchange-correlation energy which it models using the gradient of the electron density. Several notable functionals, including PW91 developed by Perdew and Wang in 1991 [98,99] and the PBE functional by Perdew, Burke and Ernzerhof constructed in 1996 [100], have been developed within the GGA framework. The generalized-gradient approximation effectively predicts properties such as lattice structures, magnetic behaviour, and elastic constants, often aligning well with experimental results across a variety of materials. However, its limitations become evident in certain areas, such as underestimating band gaps and bond lengths in semiconductors and insulators. Furthermore, it struggles to describe systems with strongly correlated electrons, like high-temperature superconductors and heavy fermion compounds. In general, LDA provides foundation for the GGA in which enhancement factor F(s) directly modifies the LDA energy as:

$$E_{xc}^{GGA}[n(\vec{r}), s] = \int n(\vec{r}) \, \epsilon_{xc}^{LDA}[n(\vec{r})] F(s) d^3 r; \text{ where } s = C \, \frac{|\nabla n(\vec{r})|}{n^{4/3} \, (r)}$$
 (2.26)

While this form generally represents GGA, it is important to note that PW91 does not strictly follow this formulation. Instead of directly using an enhancement factor F(s), PW91 utilizes a more complex integral approach to derive the exchange-correlation functional. In contrast, PBE clearly follows this formulation, defining F(s) in a way that these constraints are directly incorporated. To achieve even greater accuracy, meta-GGA and hybrid functionals were developed, which are discussed in the following sections.

2.5.3 meta-GGA functionals (SCAN, r²SCAN)

Meta-GGA functionals are other semi-local functionals that extend the GGA by integrating kinetic energy density along with the gradients and Laplacians of the electron density. These additional terms in meta-GGA enhance the ground-state properties of molecules, surfaces, and solids beyond LDA and GGA, making them valuable for studying complex materials.

The first meta-GGA functional PKZB [101] (Perdew-Kurth-Zupan-Blaha) was introduced in 1999, improving upon GGA by using kinetic energy density, enhancing atomization energies and reaction barriers, but it did not strictly satisfy exact constraints. In 2003, the TPSS [102] (Tao-Perdew-Staroverov-Scuseria) functional was developed to obey exact constraints while balancing accuracy and efficiency for both molecules and solids. In 2006 the M06-L functional [103] was introduced by Truhlar's group as a pure meta-GGA, optimized for transition metals, thermochemistry and kinetics offering further improvements in chemical

accuracy. However, a major breakthrough came in 2015 with the development of the Strongly Constrained and Appropriately Normed (SCAN) functional [104] by Sun, Ruzsinszky, and Perdew. SCAN was the first nonempirical meta-GGA that satisfied all 17 known exact constraints applicable to this class of functionals. Despite its success, SCAN introduces numerical instabilities which leads to the development of its regularized version (rSCAN) and further regularized-restored (r²SCAN) functional [105,106] to improve stability while maintaining high accuracy. The meta-GGA functional can be given as,

$$E_{xc}^{meta-GGA}[n(\vec{r})] = \int n(\vec{r}) \, \epsilon_{xc}[n(\vec{r}), \nabla [n(\vec{r})], \nabla^2 [n(\vec{r})]] d^3r \quad (2.27)$$

2.5.4 Hybrid functionals (B3LYP, HSE06)

To address the limitations of standard exchange-correlation functionals, a group of non-local hybrid functionals was developed. The term "hybrid" denotes a blend of density functional and orbital-dependent Hartree-Fock exchange energies, motivated by the exact treatment of exchange energy in Hartree-Fock. A notable example is the widely recognized empirical B3LYP functional introduced by Becke [107], which takes the form,

$$E_{xc}^{B3LYP} = E_{xc}^{LDA} + a_0(E_x^{HF} - E_x^{GGA}) + a_x(E_x^{GGA} - E_x^{LDA}) + a_c(E_c^{GGA} - E_c^{LDA})$$
 (2.28)

A new subclass of range-separated hybrid functionals has been introduced, characterized by a distance-dependent exchange mixing. These functionals employ Hartree-Fock exchange for the short-range (SR) interactions, while transitioning back to pure density functional exchange for the long-range (LR) components. One of the examples of this family of methods is the well-known HSE06 functional is given by Heyd, Scuseria, and Ernzerhof [108].

$$E_{xc}^{HSE06} = \left[\frac{1}{4}E_x^{HF}(\mu) + \frac{3}{4}E_x^{GGA}(\mu)\right]_{cp} + \left[E_x^{GGA}\right]_{LR} + E_c^{GGA} \quad (2.29)$$

The parameter μ , often around 0.2 Å⁻¹, determines the range-separation and corresponds to a characteristic distance (2/ μ), beyond which short-range interactions diminish significantly. The limit $\mu \to \infty$ leads to calculation of pure PBE-GGA calculations. The HSE06 functional has proven successful in computing accurate properties of materials in good agreement with experimental results. M. Liu et. al [109] recently conducted a comprehensive study examined 1135 materials including metals, semiconductors, and insulators to evaluate the accuracy of the HSE06 functional in predicting material properties. This study confirmed that HSE06 calculated band gaps have a mean absolute error (MAE) of 0.687 eV as compared to

experimental values, which is significantly lower than the 1.184 eV error associated with PBE calculations. Furthermore, HSE06 enhances the accuracy of formation energy predictions, which are necessary for determining thermodynamic stability of materials. While PBE systematically underestimates formation enthalpies, resulting an MAE of 0.175 eV/atom, HSE06 reduces this error to 0.147 eV/atom, providing a more precise description of material energetics.

2.6 Modelling Solid Materials with DFT

2.6.1 Electron-Ion Interactions

The exact solution of KS equations demands accurate description of external potential, V_{ext} which mimics the electron-ion interactions in solids. However, it is difficult to determine V_{ext} in solids owing to the large number of electrons and their large oscillatory behaviour near atomic nuclei. We know that the core electrons are inert and have little impact on material's physical properties while valence electrons actively participate in these phenomena and are responsible for the most of the material's properties. Therefore, DFT provides a practical approach by treating valence and core electrons separately and simplifying their influence in solid-state systems. It is imperative to expand the auxiliary KS orbitals using established basis functions for the accurate solution of KS equations. The primary methods for evaluating electron-ion interactions are the pseudopotential technique, which is discussed in following section.

2.6.2 Plane Waves and Pseudopotential Method

In general, a crystal is formed through the systematic repetition of a unit cell in three-dimensional space, creating a periodic atomic arrangement. This periodic structure imposes a recurring potential on the electrons within the crystal. By applying Bloch's theorem, the periodicity can be leveraged to simplify the solution of the KS equations. Bloch's theorem describes the electronic wavefunction in such a lattice as a combination of a plane wave and a periodic function aligned with the lattice structure. Therefore, electronic wavefunction can be written in terms of plane waves as;

$$\varphi_{n,k}(\mathbf{r}) = \sum_{G} C_{n,k+G} e^{i(K+G)\cdot \mathbf{r}} \quad (2.30)$$

where, $C_{n,k+G}$ are expansion coefficient, k is wave vector within the first Brillouin zone and G is the reciprocal lattice vector.

This equation theoretically requires an infinite number of plane waves to describe the electronic states precisely. However, in practical calculations only plane waves with lower kinetic energy contribute significantly. The kinetic energy of a plane wave (E_{kin}) is given by:

$$E_{kin} = \frac{\hbar^2}{2m} |k + G|^2 \quad (2.31)$$

In calculations utilizing the plane wave basis set only plane waves with a kinetic lower than a certain cut-off value (E_{cut}) is taken into account. A higher cutoff energy E_{cut} includes more plane waves, improving accuracy and ensuring convergence of the total energy, forces, and stress tensors. However, larger E_{cut} also increases computational cost.

In the system with tightly bound core and valence orbitals near the atomic nucleus, very rapid oscillations in the wavefunctions are required to preserve orthogonality with core orbitals. This necessitates a vast number of plane waves (high E_{cut} values) to capture the rapid variations in these regions. We know that physical properties of a material are primarily influenced by the wavefunction in the interstitial regions between atoms, rather than near the frozen core. Therefore, the wavefunction can be approximated to be smooth and slowly varying around the frozen core while still accurately reflecting the true wavefunction outside this region. These approximations result in pseudo wavefunctions that are free of nodes or abrupt changes near the core, significantly reducing the number of plane waves required to represent the wavefunction. The potentials which produce such pseudo wavefunctions are known as pseudopotentials. Therefore, pseudopotential method is highly effective for its computational efficiency and practicality among others in DFT. The schematic of pseudopotential concept is shown in Fig. (1). The blue and red color indicates the wavefunction for coulomb potential of nucleus and pseudo wavefunction, respectively. To construct pseudopotentials effectively, the following criteria must be satisfied: (1) the valence wave function should remain unchanged outside the core radius r_c , (2) the pseudo wavefunction must precisely match the true wavefunction at the core boundary, (3) both the pseudo wavefunction and its first derivative should be continuous at the boundary, and (4) the pseudo wave function should be node-free within the core [95]. The pseudo-wave functions are tailored to align with all-electron wavefunctions beyond the core radius r_c and to ensure smooth behavior within it. Numerous approaches, including norm-conserving [110], ultrasoft and projector-augmented wave pseudopotentials have been introduced over the years [111,112]. The concept of pseudopotentials enables the creation of smooth wavefunctions devoid of nodes, which can be expanded using a plane wave framework. Despite easing certain computational hurdles, the method still necessitates a significant number of plane waves to achieve precision, making it less practical. An alternative approach, known as the projector augmented wave (PAW) method [113], involves transforming the highly oscillatory wavefunctions into auxiliary wavefunctions. This transformation allows the auxiliary wavefunctions to exhibit rapid convergence when expressed as a plane-wave expansion. These smooth wavefunctions are computationally efficient and well-suited for plane-wave-based methods. The PAW method is recognized for its exceptional accuracy and has become a cornerstone in DFT calculations.

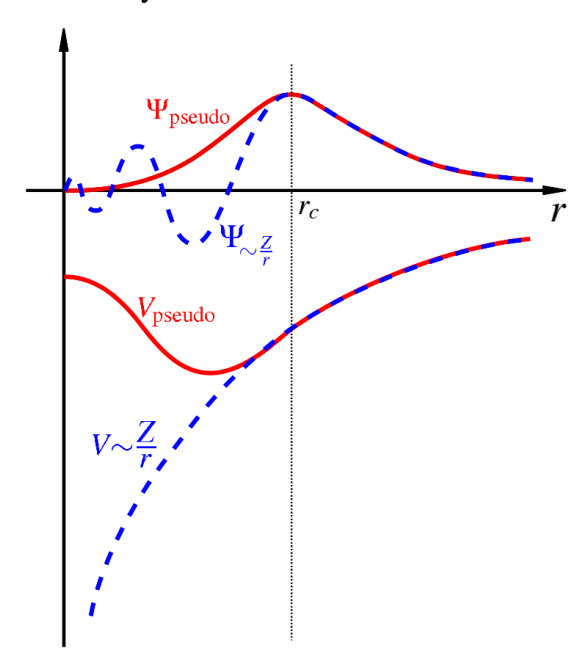


Fig. 3 A schematic illustration of the concept of pseudopotential, adapted from ref. [34]

2.6.3 van der Waals Corrections

In the conventional framework of DFT, long-range dispersion forces are not properly accounted for, which are essential for accurately calculating the adsorption behavior of molecules on surfaces and interfaces, as well as properties of molecular crystals. This limitation is particularly important for systems exhibiting quantum confinement, such as 2D materials and layered crystal structures. To address this the so-called van der Waals corrections are introduced to DFT in order to include the effects of long-range dispersion forces. Among a number of such corrections, Grimme introduced the semiempirical D2 and D3 corrections, which accurately include the long-range dispersion forces in standard DFT calculations [114–116]. The total energy after dispersion correction term is given as;

$$E_{DFT+D2/D3} = E_{KS} + E_{dis}$$
 (2.32)

where E_{KS} and E_{dis} are the energies of KS approach and Grimme's dispersion terms, respectively.

In DFT-D2 method, the dispersion energy is added as an explicit pairwise interaction between atoms:

$$E_{dis} = -s_6 \sum_{i=1}^{(N_{at}-1)} \sum_{j=i+1}^{N_{at}} \frac{c_6^{ij}}{R_{ij}^6} f_{amp} \left(R_{ij} \right) (2.33)$$

where, s_6 is a scaling factor dependent on the exchange-correlation functional, N_{at} is the total number of atoms in the system, $C_6^{ij} = \sqrt{C_6^i C_6^j}$ refers to the dispersion coefficient for an atomic pair (ij), and R_{ij}^6 signifies the distance between atoms. The $f_{dmp}(R_{ij})$ represents damping function which is given as;

$$f_{dmp}\left(R_{ij}\right) = \frac{1}{1 + e^{-d\left(\frac{R_{ij}}{R_{0ij}} - 1\right)}}$$
 (2.34)

where d is an empirical parameter and $R_{0ij} = R_{0i} + R_{0j}$ is sum of the atomic vdW radius. DFT-D3 improves upon D2 by introducing higher-order terms $(c_{8,}s_{8})$ allowing environment-dependent dispersion coefficients:

$$E_{dis} = -\sum_{i=1}^{N_{at}-1} \sum_{j=i+1}^{N_{at}} \sum_{n=6,8} s_n \frac{c_n^{ij}}{R_{ij}^n} f_{dmp,n}(R_{ij})$$
 (2.35)

Where s_6 and s_8 are scaling factors for the c_6 and c_8 terms. C_n^{ij} are dispersion coefficients that depend on the atomic coordination. $f_{dmp,n}\left(R_{ij}\right)$ is the modified damping function;

$$f_{dmp,n}\left(R_{ij}\right) = \frac{1}{1 + e^{-a_1(R_{ij}/R_{T,0}^{ij}-1)}}$$
 (2.36)

Where a_1 and a_2 are empirical parameters that influence the range of dispersion effects. $R_{r,0}^{ij}$ is a reference interatomic distance. The parameters s_8 a_1 and a_2 are optimized for different functionals by fitting to high-level quantum chemistry calculations. The values used for the HSE06 [117] and r^2 SCAN [118] are given below:

Functionals	\$8	a_1	a_2
HSE06+D3	2.310	0.383	5.685
r ² SCAN+D3	0.789	0.494	5.730

Using vdW corrections in DFT considerably increases the accuracy of calculated properties, including adsorption energies, lattice constants, and cohesive energies. It also enhances structural predictions of molecular crystals, layered materials, and van der Waals heterostructures.

2.6.4 LOBSTER: Bonding and Charge Analysis

LOBSTER first converts the delocalized wavefunctions generated from density functional theory (DFT) calculations into a localized atomic orbital basis set. It uses the projector-augmented wave (PAW) method to reconstruct local atomic orbitals, which helps in the understanding of chemical bonding. This process changes the electronic structure from a delocalized representation to a localized form which can be used for further analysis, such as using the linear combination of atomic orbitals (LCAO) approach.

After this projection, LOBSTER generates the density and the Hamiltonian matrix, which contain essential information about orbital populations and interaction strengths, allowing for a quantitative description of bonding.

The Crystal Orbital Bond Index (COBI) [119] is computed by evaluating the overlap population between two atomic orbitals across the Brillouin Zone. This measure quantifies the bonding interactions between atoms in a crystal.

$$COBI_{\mu\nu} = \sum_{i,k} w_k Re(c_{\mu,ik}^* c_{\nu,ik}) \cdot \delta(\varepsilon_i(k) - E) \quad (2.37)$$

Where $c_{\mu,jk}^*$ are the projected coefficients, w_k are the k-point weights and $\varepsilon_j(k)$ are the energy eigenvalues.

The Integrated COBI (ICOBI) is obtained by summing over all occupied energy levels. COBI corresponds to the chemical bond order, and a higher value indicate a stronger covalent interaction between atoms. For example, the ICOBI of a pair of carbon atoms in diamond is 0.95, which is close to 1 as this is the bond order expected for a single C-C bond.

$$ICOBI_{\mu\nu} = \int_{-\infty}^{\varepsilon_F} COBI_{\mu\nu} \quad (E) \text{ dE} \quad (2.38)$$

LOBSTER also computes atomic charges using Mulliken and Löwdin population analyses [120], which provide estimates of electron distribution on atoms.

The Mulliken charge on an atom A is given by:

$$q_A = N_A - \sum_{u \in A} P_u \quad (2.39)$$

Where N_A is the number of valence electrons on atom A and P_{μ} is the electron population in atomic orbitals.

Löwdin charges are computed similarly but use an orthogonalized density matrix to reduce basis-set dependencies. This method provides a more consistent charge distribution compared to Mulliken analysis.

2.7 XtalOpt: An Open-Source Tool for Crystal Structure Prediction

XtalOpt is an evolutionary algorithm (EA) that predict crystal structures by exploring the potential energy landscape using minimal input, such as chemical formula [121]. This open-source tool integrates with external optimization programs, including VASP [112,122], PWSCF [123], and GULP [124–126].

Predicting the crystal structure of materials using only their stoichiometry has been a long-standing challenge in computational materials science. The complexity arises from the high-dimensional parameter space, which includes six lattice parameters and multiple atomic positions that must be efficiently sampled to identify global minima. Traditional methods, such as chemical intuition or random structure generation often fail for complex systems. Evolutionary algorithms, inspired by natural selection processes, offer a powerful alternative by iteratively optimizing candidate structures to converge on the most stable configurations. XtalOpt employs a population-based evolutionary algorithm where individuals undergo selection, mutation, and crossover to explore the energy landscape.

XtalOpt utilizes both pure and hybrid evolutionary operators for structure generation [127–132]. Pure operators, such as crossover [133–135], strain [134,136,137], ripple, and exchange [127,129,134–137], modify lattice parameters, atomic positions, and ordering. Hybrid operators such as "stripple" (strain + ripple) and "permustrain [136]" (exchange + strain), combine these effects to enhance search efficiency and reduce duplicate structures. Below a description of the operators is given:

- **I.** Crossover: Combines two parent structures by cutting and merging their atomic configurations. The offspring's lattice dimensions are determined by a weighted average of the parental cell vectors.
- **II. Strain:** Modifies lattice vectors using a strain matrix:

$$V_{new} = V \begin{bmatrix} 1 + \varepsilon_{11} & \frac{\varepsilon_{12}}{2} & \frac{\varepsilon_{13}}{2} \\ \frac{\varepsilon_{12}}{2} & 1 + \varepsilon_{22} & \frac{\varepsilon_{23}}{2} \\ \frac{\varepsilon_{13}}{2} & \frac{\varepsilon_{23}}{2} & 1 + \varepsilon_{33} \end{bmatrix}$$
(2.40)

where ε_{ij} are random values drawn from a zero-centered normal distribution with a specified standard deviation.

III. Ripple: Introduces periodic displacements to atomic positions:

$$\Delta Z = \rho \cos(2\pi\mu x + \theta_x) \cos(2\pi\eta y + \theta_y) \quad (2.41)$$

Here, ΔZ is the displacement of an atom along the z-axis, ρ is the displacement amplitude, μ and η define periodicity and θ_x and θ_y are random phase shifts.

- **IV. Exchange:** Adjusts atomic ordering by swapping the positions of atoms of different types a specified number of times.
- V. Stripple: Combines strain and ripple to improve search diversity and avoid duplicate structures.
- VI. **Permustrain:** Integrates atomic swapping and lattice deformation to balance structural changes.

XtalOpt continuously generates and optimizes new structures without waiting for all individuals in a generation to complete their optimization. This strategy reduces bottlenecks and improves computational efficiency. To prevent stagnation in the population, XtalOpt uses a niching strategy based on direct comparisons of atomic position and lattice parameters, providing a more precise and reliable method for ensuring structural diversity. Key parameters, such as ripple amplitude, strain standard deviation and crossover contribution are carefully adjusted to enhance search efficiency. Additionally, search space constraints including lattice parameter ranges and interatomic distances, ensure that generated structures remain physically valid.

The algorithm starts with a set of random or user-specified structures. These structures are locally optimization using external codes to refine atomic positions and lattice parameters. Their stability is evaluated based on enthalpy, which is calculated as: H = U + PV, where U is the internal energy, P is pressure, and V is the volume. Structures with lower enthalpy are

more stable and are more likely to contribute to the next generation of structures via evolutionary operators. This iterative process continues until the user terminates it or reaches convergence.

XtalOpt version r12 has been integrated with a machine learning (ML) model trained on the Automatic FLOW (AFLOW) database, which introduces a multi-objective optimization approach that evaluates structural stability (enthalpy/energy) alongside mechanical properties such as bulk and shear modulus [138]. This enhancement allows the algorithm to identify superhard materials more efficiently while significantly lowering the computational cost of DFT-based elastic tensor calculations. By optimizing beyond just enthalpy minimization, this approach makes the search process faster, more flexible, and adaptable, expanding its application to properties like electronic bandgaps, superconductivity, and thermal stability.

XtalOpt has been extensively applied in high-pressure research, where chemical intuition often fails in experimental determination under extreme conditions. Ongoing development in XtalOpt is focused on improving crossover strategies and explore additional fitness metrics to improve performance. With a user-friendly interface and comprehensive tutorials, XtalOpt is accessible to researchers across various disciplines, including chemistry, physics, and materials science. One of its key applications is the prediction of high-pressure hydrides, which are interesting because of their potential as hydrogen-rich superconductors [139–141]. By facilitating the discovery of novel high-pressure materials with significant technological potential, XtalOpt continues to drive innovation across multiple scientific fields.

2.8 Phonon Structure

Lattice dynamics theory developed from the quantum harmonic oscillator, provides a systematic approach modelling atomic vibrations in periodic solids. It offers an alternative to classical empirical models and molecular dynamics (MD) simulations for studying natural thermal motion and its influence on physical properties, all while maintaining a modest computational cost [142,143].

In condensed matter physics, these atomic vibrations are known as phonons. These vibrations consist of waves created by the displacement of atoms in the crystal lattice and are classified as a type of quasiparticle. Phonons, as quasiparticles play an important role in understanding the thermal, optical, and mechanical properties of materials.

In the harmonic approximation, a crystal is represented as a network of atoms connected by harmonic springs, with its vibrations described by 3N normal modes (N is the number of atoms in the primitive unit cell). Each normal mode appears as a traveling wave [144]:

$$A \exp[i(q \cdot r - \omega t)]$$
 (2.42)

Where q is the wave vector, ω is the angular frequency and A is the vibration amplitude.

The energy with each normal mode is quantized as:

$$E_q = \left(n_q + \frac{1}{2}\right)\hbar\omega(q) \quad (2.43)$$

Where $n_q = 0,1,2,...$ and each quantum of vibrational energy $\hbar\omega(q)$, defines a phonon analogous to a photon in electromagnetic waves. Although phonons as quasiparticles do not carry true momentum but they are assigned an effective momentum $\hbar q$ for practical analysis.

The theoretical framework of phonons begins with the potential energy U(r) of a crystal, which can be expressed using a Taylor series expansion around the equilibrium atomic positions r_0 :

$$U(r) = U(r_0) + \sum_{i,\alpha} \frac{\partial U}{\partial u_{i\alpha}} u_{i\alpha} + \frac{1}{2} \sum_{i,j,\alpha,\beta} \frac{\partial^2 U}{\partial u_{i\alpha} \partial u_{j\beta}} u_{i\alpha} u_{j\beta} + \dots$$
 (2.44)

Here, $u_{i\alpha}$ represents the displacement of atom i in the α direction from equilibrium, and $U(r_0)$ is the energy of the system at equilibrium, The second term vanishes because the forces $(\partial U/\partial u_{i\alpha})$ are zero at equilibrium and the third term involving the second derivatives of U, defines the force constants $\phi_{i\alpha,j\beta}$:

$$\phi_{i\alpha,j\beta} = \frac{\partial^2 U}{\partial u_{i\alpha} \partial u_{j\beta}} \quad (2.45)$$

By neglecting higher-order terms simplifies the potential energy as a quadratic functional, which forms the basis of the harmonic approximation.

The oscillatory motion of atoms around their equilibrium positions is governed by Newton's equation of motion. For an atom i of mass M_i , displaced by u_i in the α direction, the equation of motion is:

$$M_i \frac{d^2 u_{i\alpha}}{dt^2} = -\sum_{j,\beta} \phi_{i\alpha,j\beta} u_{j\beta} \quad (2.46)$$

The solutions to these equations describe two types of vibrational modes: acoustic and optical. Acoustic modes involve low-frequency oscillations in which atoms move in phase with each other. These include longitudinal acoustic (LA) modes, where vibrations travel in the same direction as the wave, and transverse acoustic (TA) modes, where the vibrations occur perpendicular to the direction of wave propagation. In contrast, optical modes involve out-of-phase vibrations between neighboring atoms and occur at higher frequencies. These modes are important for interactions with light and play a key role in determining the material's thermal and mechanical properties.

The atomic displacements in a periodic lattice are expressed using plane wave solutions:

$$u_{i\alpha}(t) = \frac{1}{\sqrt{M_i}} e^{i(k \cdot r_i - \omega t)} \epsilon_{\alpha}(q) \quad (2.47)$$

This is the refined version of simpler plane wave expression in equation (2.42). Here $\epsilon_{\alpha}(q)$ is the polarization vector, describing the vibration direction of atoms in a specific phonon mode. The inclusion of mass M_i ensures correct normalization in phonon calculations.

Substituting the wave solution into the equation of motion leads to the dynamical matrix [145,146], which is defined as:

$$D_{\alpha\beta}(q) = \frac{1}{\sqrt{M_i M_j}} \sum_j \Phi_{i\alpha,j\beta} e^{iq \cdot (r_i - r_j)}$$
 (2.48)

The dynamical matrix D(q) is Hermitian matrix and has real eigenvalues [143]. Its diagonalization gives the squared phonon frequencies (ω^2). Positive squared frequencies ($\omega^2 > 0$) indicate dynamic stability in the system as they correspond to restoring forces. On the other hand, negative squared frequencies ($\omega^2 < 0$) correspond to the imaginary frequencies, indicating dynamical instability.

There are two methods to calculate D(q). The first is the finite-displacement method [145], where atoms are slightly shifted in real space, and the resulting forces are used to calculate the force constants. This method often requires large supercells to accurately capture long-range interatomic forces and achieve precise sampling of the Brillouin zone. The second method is based on linear-response theory, which directly calculates D(q) in reciprocal space by using density functional perturbation theory (DFPT) [147–149].

Crystal symmetry significantly reduces computational effort and improves accuracy by minimizing the number of unique atomic displacements and *q*-points, focusing on the irreducible Brillouin zone [145].

The phonon density of states (DoS) quantifies the number of vibrational modes available at each frequency ω :

$$g(\omega) = \frac{1}{N} \sum_{q} \delta(\omega - \omega(q))$$
 (2.49)

This functional is crucial for connecting microscopic phonon spectrum to macroscopic thermodynamic behavior.

The vibrational contribution to the Helmholtz free energy $F_{(vib)}$ at constant volume is given by:

$$F_{(vib)} = \frac{1}{2} \sum_{q,s} \hbar \omega_s(q) + k_B T \sum_{q,s} \ln \left[1 - e^{-\frac{\hbar \omega_s(q)}{k_B T}} \right] \quad (2.50)$$

where \hbar is the reduced Planck constant, k_B is the Boltzmann constant, T is the temperature, and $\omega_S(q)$ is the frequency of the phonon mode. Using the free energy (F) other thermodynamic properties such as heat capacity (Cv) and entropy (S) can be derived. This expression accounts for both zero-point energy and thermal occupation of phonon states.

The quasi-harmonic approximation (QHA) extends harmonic phonon theory to include temperature and pressure effects [145,150]. In this method, phonon frequencies are treated as functions of the unit cell volume (V). The Gibbs free energy in QHA is given by:

$$G(P,T) = {}^{min}_{V}[E(V) + F_{vib}(V,T) + PV]$$
 (2.51)

Where E(V) is the ground-state energy, $F_{vib}(V,T)$ is the vibrational free energy, and PV represents the pressure-volume term. By minimizing G(P,T) with respect to V, equilibrium properties such as thermal expansion and bulk modulus are determined. In this dissertation, the finite displacement method followed by QHA calculations was carried out using the Phonopy code. The typical steps in Phonopy-based phonon calculations include:

- Supercell Generation: A supercell of the crystal structure is generated to capture periodicity and interatomic interactions.
- II. **Displacement Creation:** Small displacements are applied to specific atoms, generating configurations for force calculations.
- III. **DFT Software Integration**: Input configurations into DFT software (e.g., VASP) to compute forces.
- IV. Force Constant Extraction: Use Phonopy to extract force constants $\phi_{i\alpha,j\beta}$.

V. **Dynamical Matrix Construction:** Using the force constants, the dynamical matrix is constructed, and eigenvalues are solved to obtain phonon dispersion relations.

2.9 Raman Spectroscopy

Raman spectroscopy is a widely used technique for studying vibrational properties in materials. The intensity of Raman active modes is determined by the dielectric polarizability tensor, which changes with atomic motion.

In this section, we present a systematic approach for computing Raman activities by using phonon eigenvectors from the dynamical matrix $D_{\alpha\beta}(q)$ and dielectric tensor derivatives as described in earlier theoretical frameworks [151,152].

Raman tensor is given by:

$$R_{ij}^{(s)} = \frac{\partial \alpha_{ij}}{\partial Q_s} \quad (2.52)$$

Where α_{ij} is the dielectric polarizability tensor and Q_s is the phonon normal mode coordinate.

The equation for normal mode coordinates and atomic displacements is given by:

$$Q_s = \sum_k X_k^{(s)} u_k$$
 (2.53)

Where $X_k^{(s)} = e_k^{(s)} / \sqrt{M_k}$ is the mass-weighted phonon eigenvector and u_k is the atomic displacement.

Now the Raman tensor can be rewrite as:

$$R_{ij}^{(s)} = \sum_{k} \frac{\partial \alpha_{ij}}{\partial u_k} X_k^{(s)} \quad (2.54)$$

This equation shows that the Raman tensor depends on how the dielectric polarizability changes as atomic displacements occur.

The dielectric polarizability derivatives are calculated as follows using finite differences from first-principles calculations:

$$\frac{\partial \alpha_{ij}}{\partial u_k} = \frac{\alpha_{ij}(u_k + \Delta u) - \alpha_{ij}(u_k - \Delta u)}{2\Delta u} \quad (2.55)$$

Using this approximation, the Raman tensor components are computed as:

$$R_{ij}^{(s)} = \sum_{k} \left[\frac{\alpha_{ij}(u_k + \Delta u) - \alpha_{ij}(u_k - \Delta u)}{2\Delta u} \right] X_k^{(s)} \quad (2.56)$$

Once the Raman tensor is obtained, the Raman intensity of each mode is determined by:

$$I_{Raman} = 45 \left[\frac{1}{3} (I_{11} + I_{22} + I_{33}) \right]^{2} + \frac{7}{2} \left[(I_{11} - I_{22})^{2} + (I_{11} - I_{33})^{2} + (I_{22} - I_{33})^{2} + (I_{12} + I_{13}^{2} + I_{23}^{2}) \right]$$
(2.57)

Where I_{ij} are elements of the Raman tensor. The first term represents the isotropic contribution to Raman scattering, while the second term accounts for the anisotropic contributions which influence polarization effects.

To compare theoretical Raman spectra with experimental results, a Lorentzian broadening function is applied. This accounts for phonon finite lifetimes and spectrometer resolution limits:

$$I(\omega) = \sum_{S} I_{S}^{Raman} \frac{1}{\pi} \frac{\Gamma}{(\omega - \omega_{S})^{2} + \Gamma^{2}}$$
 (2.58)

Where Γ is the phonon lifetime broadening factor which accounting for finite phonon lifetimes and instrumental resolution effects.

2.10 Mechanical Properties

Elastic properties describe how materials respond to stress or strain, offering vital insights into their brittleness, stiffness, hardness, and structural stability. These properties are influenced by external pressure and provide valuable information about phase transitions and the mechanical stability of crystal structures. Elastic constants are calculated using equilibrium configurations, where atomic positions are relaxed under each strain applied to the unit cell. The numerical derivative of energy with respect to strain helps to calculate stress, forming the basis for assessing the mechanical performance and stability of materials [153].

In the linear elastic regime, the relationship between the stress tensor (σ_{ij}) and the corresponding strain tensor (ε_{kl}) is described by Hooke's Law:

$$\sigma_{ij} = \sum_{k,l} C_{ijkl} \varepsilon_{kl} \quad (2.59)$$

where C_{ijkl} represents the elastic stiffness tensor. On the grounds of static energy analysis, the elastic constants correspond to the second derivative of energy with respect to strain per unit volume. This relationship can be expressed as:

$$C_{ijkl} = \frac{\partial^2 U}{\partial \varepsilon_{ij} \partial \varepsilon_{kl}}$$
 (2.60)

Where the stiffness tensor is represented as C_{ij} in matrix form, determined by the crystal symmetry.

In this work, the elastic constants were calculated for bromine, which has an orthorhombic crystal structure. Orthorhombic crystals exhibit nine independent elastic constants (C_{ij}):

$$C_{ij} = \begin{bmatrix} C_{11} & C_{12} & C_{13} & . & . & . & . \\ . & C_{22} & C_{23} & . & . & . & . \\ . & . & C_{33} & . & . & . & . \\ . & . & . & C_{44} & . & . & . \\ . & . & . & . & . & C_{55} & . \\ . & . & . & . & . & . & . & . \end{bmatrix}$$
(2.61)

For mechanical stability, these constants must satisfy the Born stability criteria [154,155] defined by the following relationships for orthorhombic crystals:

$$C_{ii} > 0$$
, $C_{ii} + C_{jj} - 2C_{ij} > 0$, $C_{11} + C_{22} + C_{33} + 2(C_{12} + C_{13} + C_{23}) > 0$

The C_{ij} constants define properties of single crystals. Properties of polycrystalline aggregates of crystal are described by aggregate mechanical properties. Aggregate mechanical properties such as bulk modulus (B) and shear modulus (G) are calculated from C_{ij} using averaging methods such as Voigt, Reuss, or Hill approximations [155].

The Voigt approximation assumes uniform strain and gives:

$$B_V = \frac{1}{9} [C_{11} + C_{22} + C_{33} + 2(C_{12} + C_{13} + C_{23})]$$

$$G_V = \frac{1}{15} [(C_{11} + C_{22} + C_{33} - C_{12} - C_{13} - C_{23}) + 3(C_{44} + C_{55} + C_{66})]$$

The Reuss approximation assumes uniform stress and uses elastic compliance constants (S_{ij}) , obtained as the inverse of the matrix of elastic constants.

$$B_R = \frac{1}{9} [S_{11} + S_{22} + S_{33} + 2 (S_{12} + S_{13} + S_{23})]$$

$$G_R = \frac{15}{4} \left[\frac{1}{(S_{11} + S_{22} + S_{33}) - 4 (S_{12} + S_{13} + S_{23}) + 3(S_{44} + S_{55} + S_{66})} \right]$$

The Hill approximation averages the Voigt and Reuss results:

$$B_H = \frac{B_V + B_R}{2}, \qquad G_H = \frac{G_V + G_R}{2}$$

Using these moduli, other mechanical properties such as Young's modulus (E) and Poisson's ratio (ν) can also be calculated.

Young's modulus (E), describes the material's rigidity, is calculated as:

$$E = \frac{9GB}{3B + G}$$

Poisson's ratio, indicating the material's ductility, is given by:

$$v = \frac{3B - 2G}{2(3B + G)}$$

These properties provide a comprehensive understanding of the material's mechanical behavior and are crucial for predicting its performance under various conditions.

3. Summary of Results

The work presented in this thesis has been published in three articles and one unpublished manuscript (currently under review), all of which are listed in Section 1.6 of the Introduction and included as Appendices. This section provides a comprehensive summary and discussion of the main results, focusing on the behavior of halogens, particularly bromine and fluorine under high-pressure conditions.

3.1 High-Pressure Behavior of Solid Bromine

We started our research by investigating the high-pressure behavior of solid bromine using hybrid DFT calculations. Traditional GGA-based methods struggle to accurately describe phase transitions and electronic properties of such systems at extreme pressures, necessitating a more advanced approach. To improve accuracy, we employed DFT calculations with the HSE06 functional and Grimme-D3 dispersion correction, utilizing VASP 6.2 code to study the structural and electronic properties of bromine up to 200 GPa. For these calculations, we used standard PAW potentials, explicitly treating the $4s^2/4p^5$ valence electrons. A plane-wave energy cutoff of 800 eV was applied and the Brillouin zone was sampled using a Monkhorst-Pack mesh with a k-point spacing of $2\pi \times 0.033 \text{Å}^{-1}$. Electronic minimization was performed with a convergence threshold of 10^{-7} eV. Structural optimizations were performed until atomic forces were reduced below 5 meV/Å, ensuring accurate assessment of metallization, phase stability, and incommensurate phases. Additionally, we employed Lobster 4.1.0 for bonding analysis, VESTA for structural visualizations, and FINDSYM for symmetry recognition.

At ambient pressure, both GGA and meta-GGA methods predict the ground-state structures of iodine and bromine incorrectly, favoring C2/m monoatomic chains over the experimentally observed molecular Cmca phase. To resolve this, we applied several functionals with D3 dispersion corrections (see Table 1 in the Supplementary Material of article A1, Appendix 1). Our results shows that the only hybrid functionals correctly reproduced the energetic stability of the Cmca phase, with structural accuracy improving from GGA to meta-GGA to hybrid methods (see below Fig. 4). We therefore adopted hybrid functionals for further calculations. Comparisons of theoretical lattice constants and Raman frequencies with experimental X-ray and vibrational spectroscopic data show excellent agreement (see Fig. 3 in article A1, Appendix 1), confirming that our calculations accurately capture the high-pressure stability of the molecular Cmca phase.

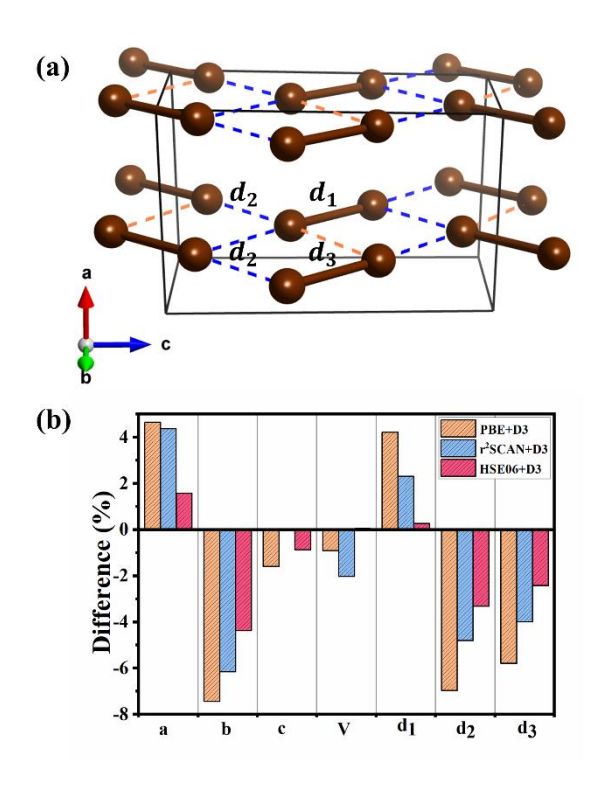


Fig 4. (a) Crystal structure of solid bromine in the Cmca molecular structure (Phase I). (b) Comparison between the computed and experimentally observed geometry of the Cmca phase at 1 atm.

Our results confirm that solid bromine undergoes a pressure-induced phase transition from the Cmca (molecular) $\xrightarrow{90~GPa}$ Immm (nonmolecular) phase. This result closely aligns with previous experimental studies, which reported this transition around 80 ± 5 GPa [52].

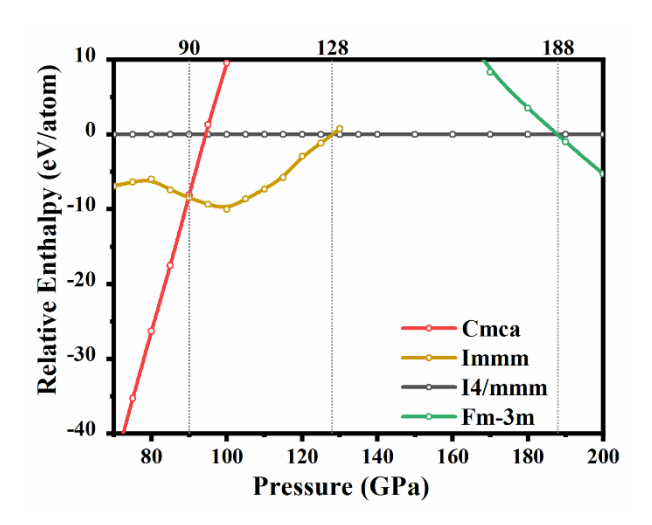


Fig 5. Pressure-dependent enthalpies (at T = 0 K) of bromine phases relative to the I4/mmm structure.

Additionally, our calculation predicts two further phase transitions that at the time of publication have not yet been observed experimentally from $Immm \xrightarrow{128 GPa} I4/mmm$ $\xrightarrow{188 GPa} Fm\overline{3}m \text{ as shown in above Fig.5.}$

A significant result of our study is that bromine becomes metallic at 80 GPa while still in its molecular Cmca phase. Previous GGA-based calculations predicted metallization at a much lower pressure of 42.5 GPa [58] (see Fig.5 from article A1, Appendix 1). This metallization occurs due to the weakening of the Br-Br bond, driven by increasing antibonding effects due to the shortening of intermolecular Br···Br contacts under compression. As the molecular bond destabilized, bromine transitions into quasi-2D metallic structures (Immm and I4/mmm) before finally adopting a fully 3D metallic face-centered cubic ($Fm\bar{3}m$) structure at 188 GPa, as depicted in below Fig. 6.

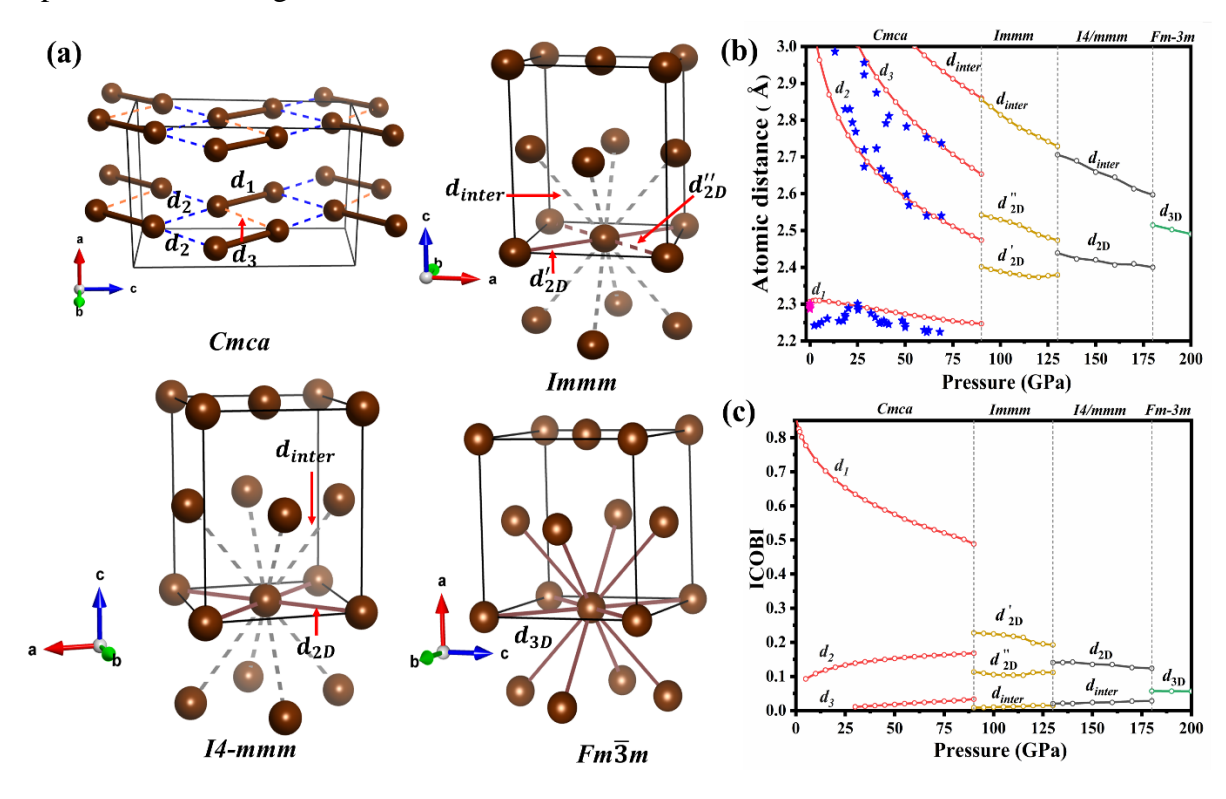


Fig 6. (a) High-pressure crystal structures of solid bromine: phase I (Cmca), phase II (Immm), phase III (I4/mmm), and phase IV (Fm\(\overline{3}\)m). (b) Br-Br distances calculated as a function of pressure for all four phases. Stars indicate experimental values (blue-ref. [156] pink – ref. [157]). (c) Integrated crystal orbital bond index (ICOBI) for Br-Br distances. The vertical dashed lines in (b) and (c) represent the predicted pressures for structural transitions between the respective ground-state phases of bromine.

Another intriguing aspect of bromine high-pressure behavior is the appearance of incommensurate phases during its transition from *Cmca* to *Immm*. Our study indicated that the *Fmm2-28* structure remains stable only within a narrow pressure range of 89 to 92 GPa, while

the *Cm-10* phase never becomes energetically favorable at any pressure (see Fig.6 in article A1, Appendix 1). These modulated phases appear to be transient intermediates which are most probably stabilized to the entropic terms which are not included in our calculations. Recent single-crystal synchrotron X-ray diffraction (SCXRD) studies by Yin et al. [50] have experimentally confirmed the presence of incommensurate structures in bromine within the 81–112 GPa pressure range, validating our theoretical predictions. Further details are provided in article A1 (Appendix 1).

3.2 Stability and Reactivity of Bromine Fluorides

Beyond pure bromine, we extended our investigation to bromine fluorides under compression. Fluorination is known to significantly alter the bonding behavior of halogens, and our goal was to explore the stability and reactivity of bromine fluorides at high pressures.

We explored the stability and reactivity of bromine fluorides up to 100 GPa, focusing on how compression influences their bonding and phase transitions. The enthalpy and geometry of BrF were calculated at T=0 K using VASP 6.3 codes. The standard PAW potentials were used with explicit treatment of the $4s^2/4p^5$ electrons of bromine and the $2s^2/2p^5$ electrons of fluorine. For all calculations, we used a plane-wave energy cutoff of 800 eV and electronic minimization was considered converged when energy differences reached 10^{-7} eV. The Brillouin zone was sampled using a Monkhorst–Pack mesh, with a $2\pi \times 0.033\text{Å}^{-1}$ spacing of k-points. The electron localization function (ELF) was computed using VASP, while additional analyses, including phonon dispersion, bonding analysis, structural visualization, and symmetry recognition, were carried out with Phonopy, Lobster 4.1.0, VESTA, and FINDSYM.

Additionally, a structure search was performed using XtalOpt (version r12) to explore the lowest-enthalpy structures of bromine fluorides (Br_mF_n , where m=1, n=1-7, and m=2, n=3, 5) at 20, 50, and 80 GPa. The searches used structures in which the number of formula units per unit cell was between 1 and 6. The initial generation consisted of 18 randomly generated structures, with additional seed structures included from previous calculations. Symmetry constraints and space group perception with a length tolerance of 0.150 Å ensured structural diversity while avoiding duplicates. The search used an evolutionary algorithm with a pool size of 20 structures per formula unit allowing up to 25 continuous structures per generation. The first-generation structures were evolved using a combination of crossover (15%), stripple mutations (50%), permutations (35%), and lattice strain mutations (maximum strain standard deviation of 0.5). Formula unit crossovers were introduced after generation 4. A total of 399

structures per search were generated during the search, with up to 24 jobs running in parallel to optimize computational efficiency. The fitness function used for selecting the most stable structure was based on enthalpy minimization and evaluated using DFT calculations with the r²SCAN+D3 functional.

Our calculations confirmed the stability of BrF₃ and BrF₅ at ambient pressure and also predicted two novel bromine fluorides BrF₂ and BrF₆ under high-pressure conditions.

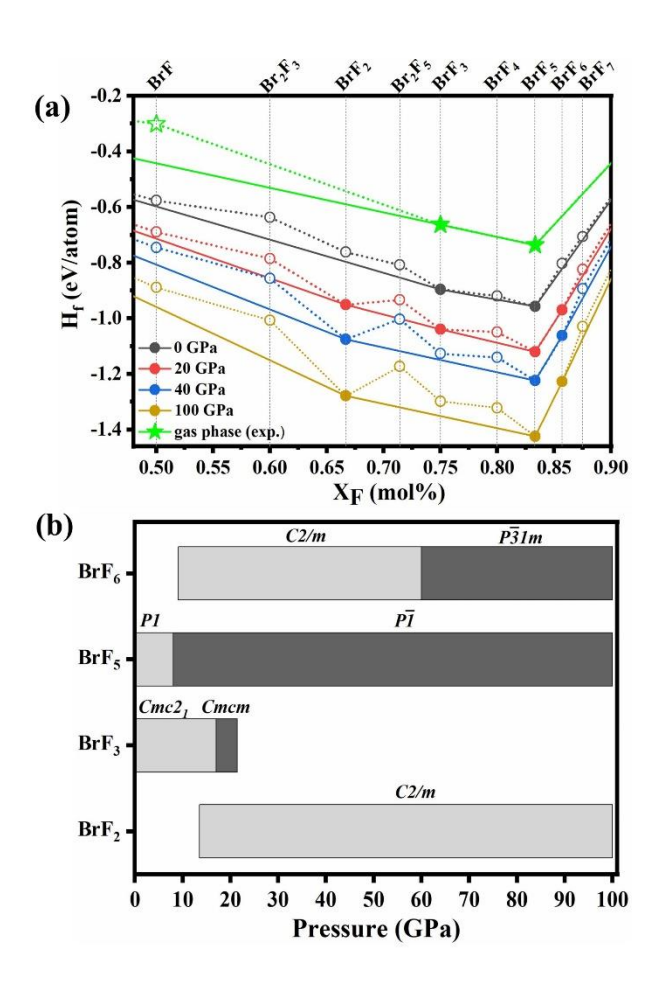


Fig 7. Convex hull diagram predicting the stability for bromine fluorides at different pressures (filled symbols represent stable stoichiometries); experimental formation enthalpies for gaseous BrF (green stars) are from ref. [158] (b) Br-F phase diagram (0 atm to 100 GPa) with colors and symmetry labels for stable phases.

BrF₃ undergoes a pressure-induced phase transition from $Cmc2_1 \xrightarrow{17 GPa} Cmcm \xrightarrow{26 GPa} P\overline{1}$. It is important to note that, BrF₃ becomes thermodynamically unstable above 21 GPa with respect to decomposition into BrF₅ and the newly predicted bromine fluoride of BrF₂.

Enthalpy formation calculations, depicted in Fig. 7(a), indicate that BrF₅ is the most stable bromine fluoride in the studied pressure range. BrF₅ exists as a liquid under ambient conditions, but it crystallizes into a solid phase with *P1* symmetry at 1 atm. Around 8 GPa, it transforms

into a molecular crystal with $P\overline{1}$ symmetry, consisting of square pyramidal BrF₅ units. In the P1 phase at ambient pressure, Br-F bond lengths range from 1.72 to 1.83 Å, while in the $P\overline{1}$ phase at 100 GPa, the bond lengths are slightly shorter, ranging from 1.65 to 1.81 Å (see Fig. S3 in supplementary material of article A2, Appendix 2). Notably, BrF remains thermodynamically unstable across the entire pressure range of 0 to 100 GPa.

BrF₂ emerges as novel bromine fluoride, becoming thermodynamically and dynamically stable at pressures above 13 GPa and remaining stable up to at least 100 GPa. It adopts a monoclinic *C2/m* crystal structure, characterized by a distinct trimeric arrangement of F-Br-F units, where the central unit is linear and the outer ones are slightly bent (see Fig. 5, article A2, Appendix 2). This unique trimeric configuration is stabilized by three-center bonding interactions between bromine atoms, which leads to the formation of radical species. BrF₂ is also predicted to be an open-shell, semiconducting compound with a small but finite band gap that persists even under high pressure. Importantly, it may be synthesized either by the reaction of Br₂ and BrF₃ at 13 GPa or through the pressure-induced decomposition of BrF₃ into BrF₂ and BrF₅ above 21 GPa, offering experimentally accessible routes to this novel compound.

Similarly, BrF₆ became stable above 9 GPa and persisted on the convex hull up to 100 GPa, as illustrated in Fig. 7(a). BrF₆ stabilizes through an alternative pathway, with its electrons more uniformly delocalized across the molecule, resulting in a more stable electronic structure. These results show how applying high pressure changes the behavior of bromine fluorides, making them structurally and electronically different from iodine fluorides. Further details and an extended discussion of these results are available in article A2 (Appendix 2).

3.3 Thermal and Mechanical Behaviour of Bromine under High Pressure

To explore the thermal and mechanical properties of bromine under high pressure, we performed hybrid DFT calculations in combination with the quasi-harmonic approximation (QHA). Phonon dispersion analysis using the finite displacement method (Phonopy 2.18.0) confirmed that the *Cmca* phase remains dynamically stable up to 90 GPa, with no signs of imaginary vibrational modes (see Fig. 2 in article A3, Appendix 3).

The calculated Raman-active frequencies closely match with experimental results as shown in Fig.8a. DFT modeling accurately captures the $2A_g$ and $2B_{3g}$ frequency shift above 20 GPa and the significant hardening of the $1A_g$ and $1B_{3g}$ librational modes, which increase by over 100 cm^{-1} at 30 GPa. These hindered rotations within the bc plane (Fig. 8b) have higher frequencies and greater pressure dependence than the $1B_{1g}$ mode.

The computed Raman spectra for the Cmca phase (Fig.8c) shows negligible $1B_{1g}$ and $1B_{2g}$ mode intensity at 0 GPa, explaining their absence in experiments. As shown in Fig. 8d, their intensity increases with pressure, which is consistent with the observed emergence of $1B_{1g}$ above 30 GPa. Additionally, the pressure-induced increase in $1A_g$ intensity obscures the $2B_{2g}$ band, explaining its absence in experimental observations.

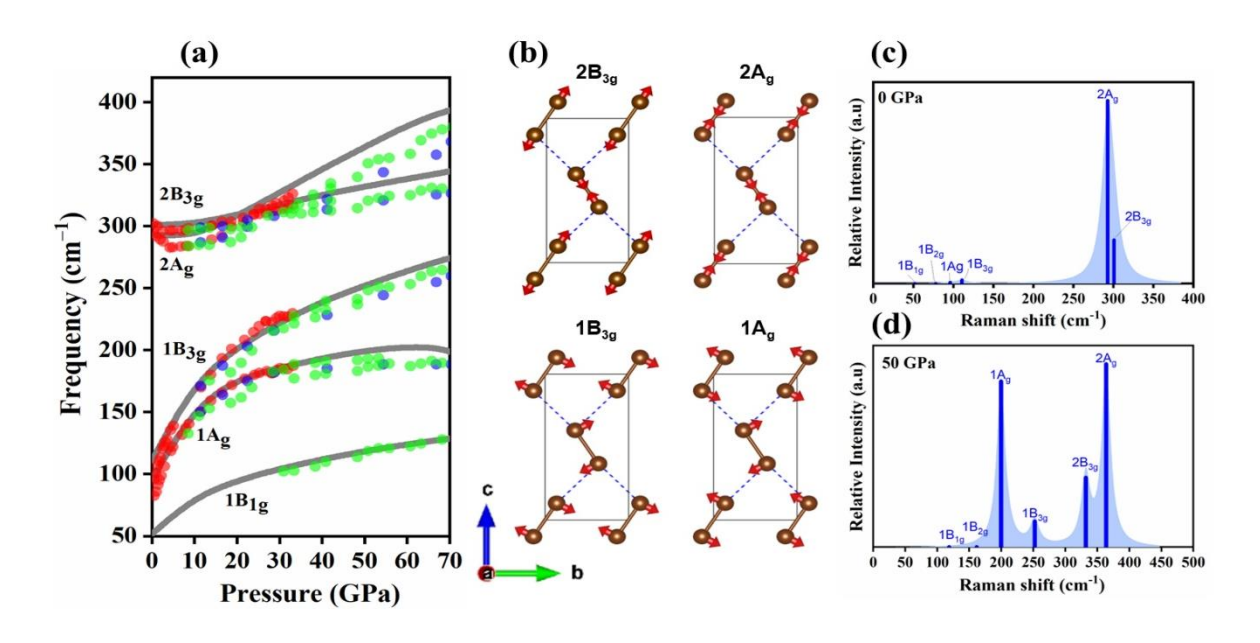


Fig 8. (a) Raman frequencies for the Cmca phase: our HSE06+D3 data (grey lines) and experiment (dots, red—ref. [159], green—ref. [160], blue—ref. [54]). (b) Atomic displacements (red vectors) in the B_{3g} and A_g modes. (c, d) calculated Raman spectra of bromine (blue lines) at 0 GPa and 50 GPa.

Using phonon based QHA calculations, we derived thermodynamic parameters such as free energy (F), entropy (S), heat capacity, and thermal expansion coefficients across a temperature range from 0 to 1000 K and pressures up to 90 GPa (see Fig.4 from article A3, Appendix 3). Our results show that the heat capacity initially follows the T^3 dependence predicted by Debye theory at low temperatures. As pressure increases, the heat capacity approaches the Dulong–Petit limit but at a higher temperature, reflecting enhanced intermolecular interactions and anharmonic effects. The thermal expansion coefficient (α) also decreases with pressure, reflecting the increased rigidity of the molecular structure of bromine under compression.

The calculated elastic constant indicate that the C₁₃ begins to soften around 60 GPa while C₄₄ elastic constant decreases above 80 GPa (see below Fig.9). This trend suggests mechanical instability near 90 GPa, coinciding with predicted band gap closure (~80 GPa) and experimentally determined appearance of incommensurate phases (~81 GPa) [50].

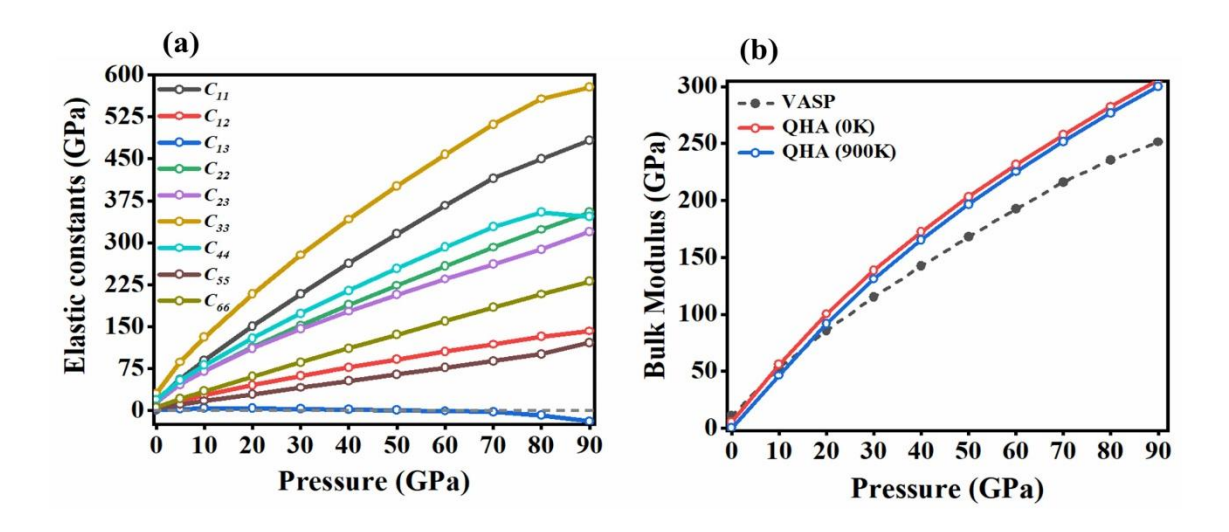


Fig 9. The pressure dependence of (a) the calculated elastic constants at 0 K and (b) the bulk modulus, with a comparison between VASP and OHA for bromine.

We also examined pressure-dependent isotropic bulk modulus (B), shear modulus (G), and Young's modulus (Y) of bromine using Voigt-Reuss-Hill approximation, as detailed in Section 2.10 of the Methods. At ambient pressure, the bulk modulus estimated from the elastic constants is ~11.8 GPa, which is higher than the 5.5 GPa obtained through QHA calculations, as shown in above Fig. 9b. The calculated shear and Young's moduli increase consistently with increasing pressure. At 30 GPa, the elastic modulus of bromine reaches a value comparable to that of steel (see Fig.7 article A3, Appendix 3). Furthermore, the calculated Pugh's ratio (B/G < 1.75) and Poisson's ratio (θ < 0.26) indicate that bromine is brittle in the orthorhombic phase. A comprehensive analysis of the thermal and mechanical properties of bromine up to 90 GPa is presented in article A3 (Appendix 3).

3.4 High-Pressure Behaviour of Solid Bromine - Experimental Validation

To confirm our predicted phase transitions above 90 GPa, our experimental collaborators conducted high-pressure experiments on solid bromine using diamond anvil cells (DACs), achieving static pressures up to 230 GPa. These experiments were performed at the Advanced Photon Source (USA) and the European Synchrotron Radiation Facility (France), utilizing synchrotron X-ray diffraction to examine the structural evolution of bromine under extreme conditions.

To further understand the structural changes observed in experiment, we performed additional DFT calculations to investigate the ground-state properties and potential energy surface (PES) of metallic bromine at pressures between 90 and 180 GPa. These calculations

were performed using the HSE06+D3 functional in VASP 6.3.2 code with a dense k-point sampling of $19\times19\times12$ to ensure high accuracy.

All three structure Immm, I4/mmm and $Fm\overline{3}m$ represented within common orthorhombic conventional cell by adjusting the ratios of the lattice parameters b/a and c/a, with keeping bromine atoms fixed at the fractional coordinates (0,0,0) and $(\frac{1}{2},\frac{1}{2},\frac{1}{2})$. At each pressure point, we generated a set of structures by varying b/a from 1.00 to 1.10 and c/a from 1.40 to 1.95, optimizing the cell volume at each step. When b/a = 1, the a and b axes become equal and structure becomes tetragonal, corresponding to the I4/mmm phase. Further increasing $c/a = \sqrt{2}$, leads to the cubic $(Fm\overline{3}m)$ phase, where all three lattice parameters are equal. This approach allows all three phases to be explored within a same structural framework.

For every such distortion, the unit cell volume was optimized while keeping the cell shape (i.e., b/a and c/a ratios) fixed. The enthalpy was then computed using DFT, providing a set of values that define the potential energy surface (PES) as a function of lattice shape at a given pressure. The thermodynamically stable structure corresponds to the minimum on this PES. To simplify the mapping analysis, we assumed that the system is symmetric with respect to the exchange of the a and b axes that is, H(a,b,c) = H(b,a,c).

Our X-ray diffraction data confirm that bromine undergoes a structural transition from $Immm \rightarrow I4/mmm \rightarrow Fm\overline{3}m$ phase (see Fig.1 in unpublished article A4, Appendix 4), consistent with our theoretical predictions as shown in Fig.5. However, instead of a sharp transition, experimental data show a coexistence of Immm and I4/mmm phases between 105 and 163 GPa (see Fig. S1 in supplementary material of unpublished article A4, Appendix 4). This coexistence suggests significant anharmonic and entropic contributions, indicating that both phases remain thermodynamically accessible across a broad pressure range, rather than undergoing a conventional first-order transition.

Fig. 10 shows calculated enthalpy surface of bromine as a function of b/a and c/a ratio. This contour map shows the relative enthalpies of various distortions structure, with local minima corresponding to energetically favorable phases. At 100 GPa the I4/mmm structure is a saddle point between two PES minima corresponding to the Immm structure. Starting from 120 GPa a broad, shallow region on the potential energy surface develops, encompassing both the Immm and I4/mmm structures. This reveals a high degree of anharmonicity and suggesting entropic stabilization of intermediate distortions. As pressure increases, a deeper and sharper minimum emerges around the I4/mmm configuration, marking its evolution into the thermodynamic ground state. At pressures above 160 GPa, a new minimum appears at b/a = 1 and $c/a = \sqrt{2}$,

corresponding to the $Fm\overline{3}m$ structure (see Fig. 3 in unpublished article A4, Appendix 4). Between 180 and 195 GPa, the $Fm\overline{3}m$ minimum becomes slightly lower in enthalpy than the I4/mmm, marking the onset of a transition to a fully isotropic cubic phase.

Unlike iodine [161], which undergoes a $Immm \rightarrow I4/mmm$ transition without a noticeable volume change, bromine exhibits a clear volume discontinuity, despite the symmetry relationship between these phases. Potential energy surface (PES) calculations reveal strong anharmonicity in the Immm phase, where minor lattice variations ($\sim 5-10\%$) result in minimal enthalpy changes (< 5 meV/atom). Bromine completes its structural transition with $Fm\overline{3}m$ phase, which begins around 172 GPa and fully stabilizes near 180 GPa. A detailed discussion, including the enthalpy landscape, is presented in unpublished article A4 (Appendix 4).

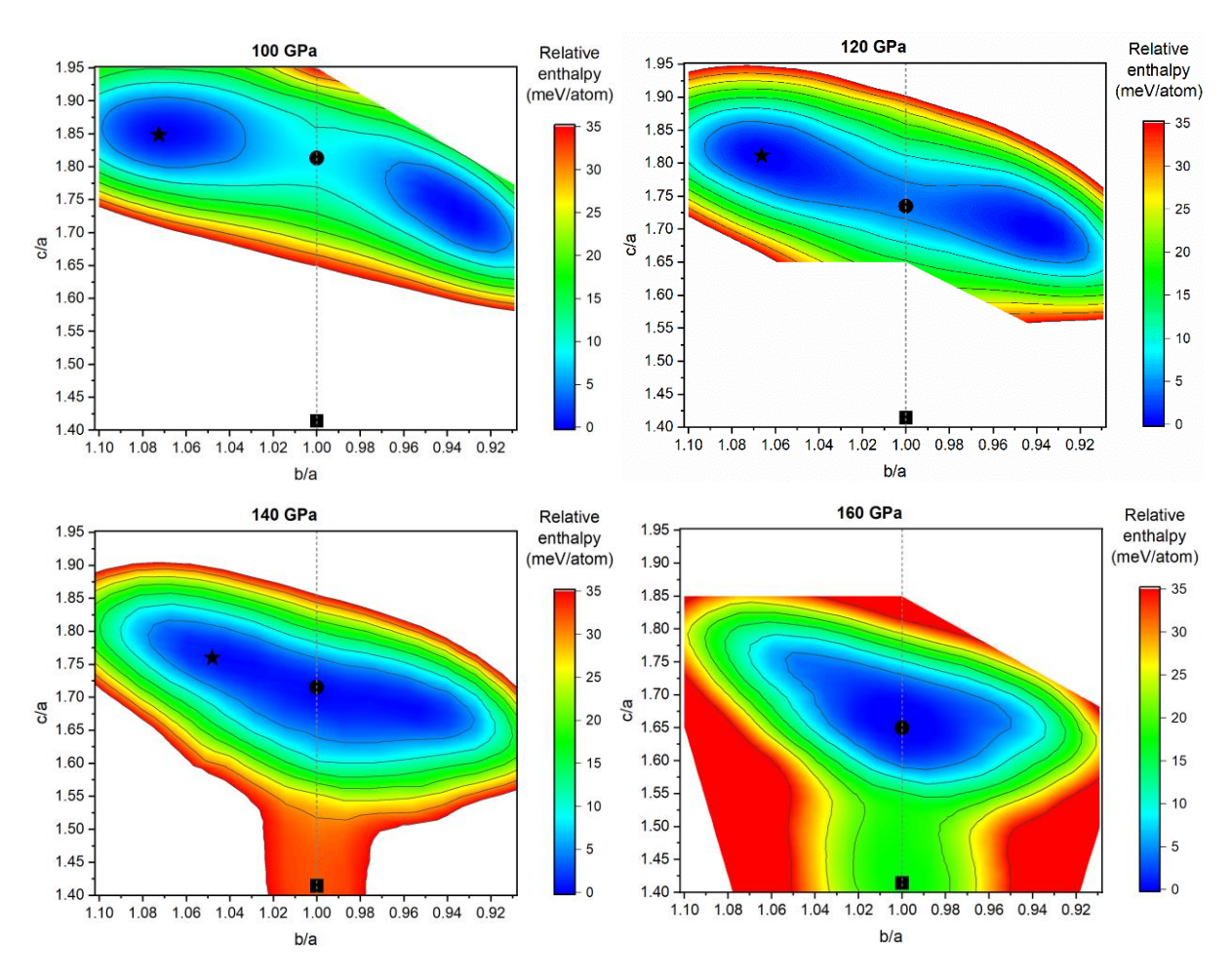


Fig 10. Pressure-dependent PES of bromine (meV/atom) as a function of c/a and b/a ratios. (Black stars indicate the Immm structure minima, black circle denoted the I4/mmm structure where b/a=1 and black square show the Fm $\overline{3}$ m structure with b/a = 1 and c/a = $\sqrt{2}$ = 1.41)

4. Conclusion and Future Work

This study presents a comprehensive theoretical and experimental investigation into the high-pressure behavior of solid bromine (Br₂), offering significant insights with high accuracy into phase pressure induced phase transformations. We examined a sequence of structural transitions between atomic phases by utilizing *state-of-the-art* computational methods, particularly hybrid density functional theory (HSE06+D3) with synchrotron X-ray diffraction. These transitions lead finally to the formation of a close-packed face centered cubic (*fcc*) bromine phase with electronically isotropic metallic characteristic. The observed phase transformation sequence is similar to the iodine but occurs at significantly higher pressures and suggesting an unexpected first-order transition. This transition was further confirmed through thermodynamic analyses based on the quasi-harmonic approximation (QHA), including mechanical stability.

Additionally, our calculations also show that the Br/F phase diagram exhibits a rich and previously unexplored chemistry under moderate pressure (~15 GPa). We found two novel bromine fluoride compounds BrF₂ and BrF₆, both open-shell, non-metallic compounds. These findings contribute to the understanding of chemical bonding and phase stability in condensed matter systems under extreme conditions.

Future research will focus on fluorine's high-pressure reactivity with other electronegative nonmetals such as oxygen, sulfur, and chlorine. In parallel, we also intend to explore nitrogenrich materials, particularly those involving $[N_2]^{x-}$ dimers and extended nitrogen structures, including recently synthesized polynitrides. This will involve a detailed analysis of bonding characteristics, N-N distances, charge distributions, and bonding indices such as the Integrated Crystal Orbital Bond Index (ICOBI). These analyses will contribute to a deeper understanding of nitrogen chemistry under extreme conditions and holds promise for the design and development of advanced materials with tailored properties for a range of technological applications.

In conclusion, this study establishes a solid foundation for understanding non-metallic bonding behavior in molecular crystals of interest under pressure and opens new pathways for discovery of unconventional compounds. It not only enhances our knowledge of elemental chemistry in extreme environments but also lays the groundwork for future experimental validation and potential technological innovations.

References

- [1] H. Mao and R. J. Hemley, *The High-Pressure Dimension in Earth and Planetary Science*, Proc. Natl. Acad. Sci. **104**, 9114 (2007).
- [2] T. S. Duffy and R. F. Smith, *Ultra-High Pressure Dynamic Compression of Geological Materials*, Front. Earth Sci. **7**, 1 (2019).
- [3] M. Miyahara, N. Tomioka, and L. Bindi, *Natural and Experimental High-Pressure, Shock-Produced Terrestrial and Extraterrestrial Materials*, Prog. Earth Planet. Sci. **8**, (2021).
- [4] Y. Song, W. Luo, Y. Wang, and C. Jin, *Unveiling the Enigma of Matter under Extreme Conditions: From Planetary Cores to Functional Materials*, Sci. Rep. **13**, 18340 (2023).
- [5] C. S. Yoo, Chemistry under Extreme Conditions: Pressure Evolution of Chemical Bonding and Structure in Dense Solids, Matter Radiat. Extrem. 5, (2020).
- [6] L. Zhang, Y. Wang, J. Lv, and Y. Ma, *Materials Discovery at High Pressures*, Nat. Rev. Mater. **2**, 1 (2017).
- [7] N. W. Ashcroft, *Metallic Hydrogen: A High-Temperature Superconductor?*, Phys. Rev. Lett. **21**, 1748 (1968).
- [8] M. I. Eremets, A. G. Gavriliuk, I. A. Trojan, D. A. Dzivenko, and R. Boehler, *Single-Bonded Cubic Form of Nitrogen*, Nat. Mater. **3**, 558 (2004).
- [9] M. Xu, Y. Li, and Y. Ma, *Materials by Design at High Pressures*, Chem. Sci. **13**, 329 (2022).
- [10] W. Grochala, R. Hoffmann, J. Feng, and N. W. Ashcroft, *The Chemical Imagination at Work InVery Tight Places*, Angew. Chemie Int. Ed. **46**, 3620 (2007).
- [11] A. P. Drozdov, M. I. Eremets, I. A. Troyan, V. Ksenofontov, and S. I. Shylin, Conventional Superconductivity at 203 Kelvin at High Pressures in the Sulfur Hydride System, Nature **525**, 73 (2015).
- [12] A. P. Drozdov, P. P. Kong, V. S. Minkov, S. P. Besedin, M. A. Kuzovnikov, S. Mozaffari, L. Balicas, F. F. Balakirev, D. E. Graf, V. B. Prakapenka, E. Greenberg, D. A. Knyazev, M. Tkacz, and M. I. Eremets, *Superconductivity at 250 K in Lanthanum Hydride under High Pressures*, Nature 569, 528 (2019).
- [13] Y. Tian, B. Xu, D. Yu, Y. Ma, Y. Wang, Y. Jiang, W. Hu, C. Tang, Y. Gao, K. Luo, Z. Zhao, L.-M. Wang, B. Wen, J. He, and Z. Liu, *Ultrahard Nanotwinned Cubic Boron Nitride*, Nature **493**, 385 (2013).
- [14] B. Cai, J. Li, H. Sun, L. Zhang, B. Xu, W. Hu, D. Yu, J. He, Z. Zhao, Z. Liu, and Y.

- Tian, Enhanced Thermoelectric Performance of Na-Doped PbTe Synthesized under High Pressure, Sci. China Mater. **61**, 1218 (2018).
- [15] R. J. Hemley, *Percy W. Bridgman's Second Century*, High Press. Res. **30**, 581 (2010).
- [16] C. E. Wehrenberg, D. McGonegle, C. Bolme, A. Higginbotham, A. Lazicki, H. J. Lee, B. Nagler, H.-S. Park, B. A. Remington, R. E. Rudd, M. Sliwa, M. Suggit, D. Swift, F. Tavella, L. Zepeda-Ruiz, and J. S. Wark, *In Situ X-Ray Diffraction Measurement of Shock-Wave-Driven Twinning and Lattice Dynamics*, Nature 550, 496 (2017).
- [17] A. F. Goncharov, *Raman Spectroscopy at High Pressures*, Int. J. Spectrosc. **2012**, 1 (2012).
- [18] B. Koneru, J. Swapnalin, P. Banerjee, K. C. B. Naidu, and N. S. Kumar, *Materials under Extreme Pressure: Combining Theoretical and Experimental Techniques*, Eur. Phys. J. Spec. Top. **231**, 4221 (2022).
- [19] M. Lewandowska and K. J. Kurzydlowski, *Recent Development in Grain Refinement by Hydrostatic Extrusion*, J. Mater. Sci. **43**, 7299 (2008).
- [20] J. Roberts and E. Zurek, *Computational Materials Discovery*, J. Chem. Phys. **156**, (2022).
- [21] K. P. Hilleke, T. Bi, and E. Zurek, *Materials under High Pressure: A Chemical Perspective*, Appl. Phys. A Mater. Sci. Process. **128**, 1 (2022).
- [22] T. Ruoko, M. Stoeckel, R. Puttreddy, C. Yang, S. Zhang, Z. Wu, N. R. Candeias, P. Samorì, H. Y. Woo, S. Fabiano, and A. Priimagi, *Halogen Bonding as a Tool to Control Morphology and Charge Transport in Organic Semiconductors*, Angew. Chemie Int. Ed. (2025).
- [23] G. Xiao, T. Geng, and B. Zou, *Emerging Functional Materials under High Pressure toward Enhanced Properties*, ACS Mater. Lett. **2**, 1233 (2020).
- [24] E. Wigner and H. B. Huntington, *On the Possibility of a Metallic Modification of Hydrogen*, J. Chem. Phys. **3**, 764 (1935).
- [25] W. Grochala, R. Hoffmann, J. Feng, and N. W. Ashcroft, *The Chemical Imagination at Work in Very Tight Places*, Angew. Chemie Int. Ed. **46**, 3620 (2007).
- [26] W. M. Awad, D. W. Davies, D. Kitagawa, J. Mahmoud Halabi, M. B. Al-Handawi, I. Tahir, F. Tong, G. Campillo-Alvarado, A. G. Shtukenberg, T. Alkhidir, Y. Hagiwara, M. Almehairbi, L. Lan, S. Hasebe, D. P. Karothu, S. Mohamed, H. Koshima, S. Kobatake, Y. Diao, R. Chandrasekar, H. Zhang, C. C. Sun, C. Bardeen, R. O. Al-Kaysi, B. Kahr, and P. Naumov, *Mechanical Properties and Peculiarities of Molecular Crystals*, Chem. Soc. Rev. 52, 3098 (2023).

- [27] D. Braga, L. Casali, and F. Grepioni, *The Relevance of Crystal Forms in the Pharmaceutical Field: Sword of Damocles or Innovation Tools?*, Int. J. Mol. Sci. 23, 9013 (2022).
- [28] M. I. Eremets, A. P. Drozdov, P. P. Kong, and H. Wang, *Semimetallic Molecular Hydrogen at Pressure above 350 GPa*, Nat. Phys. **15**, 1246 (2019).
- [29] J. M. McMahon and D. M. Ceperley, *Ground-State Structures of Atomic Metallic Hydrogen*, Phys. Rev. Lett. **106**, 2 (2011).
- [30] R. T. Howie, C. L. Guillaume, T. Scheler, A. F. Goncharov, and E. Gregoryanz, *Mixed Molecular and Atomic Phase of Dense Hydrogen*, Phys. Rev. Lett. **108**, 1 (2012).
- [31] E. Gregoryanz, C. Ji, P. Dalladay-Simpson, B. Li, R. T. Howie, and H. K. Mao, *Everything You Always Wanted to Know about Metallic Hydrogen but Were Afraid to Ask*, Matter Radiat. Extrem. **5**, (2020).
- [32] H. C. Yang, K. Liu, Z. Y. Lu, and H. Q. Lin, First-Principles Study of Solid Hydrogen: Comparison among Four Exchange-Correlation Functionals, Phys. Rev. B **102**, 174109 (2020).
- [33] P. Dalladay-Simpson, R. T. Howie, and E. Gregoryanz, *Evidence for a New Phase of Dense Hydrogen above 325 Gigapascals*, Nature **529**, 63 (2016).
- [34] M. I. Eremets, R. J. Hemley, H. K. Mao, and E. Gregoryanz, *Semiconducting Non-Molecular Nitrogen up to 240 GPa and Its Low-Pressure Stability*, Nature **411**, 170 (2001).
- [35] X. Wang, Y. Wang, M. Miao, X. Zhong, J. Lv, T. Cui, J. Li, L. Chen, C. J. Pickard, and Y. Ma, *Cagelike Diamondoid Nitrogen at High Pressures*, Phys. Rev. Lett. **109**, 1 (2012).
- [36] J. Sun, M. Martinez-Canales, D. D. Klug, C. J. Pickard, and R. J. Needs, *Stable All-Nitrogen Metallic Salt at Terapascal Pressures*, Phys. Rev. Lett. **111**, 1 (2013).
- [37] J. Sun, M. Martinez-Canales, D. D. Klug, C. J. Pickard, and R. J. Needs, *Persistence and Eventual Demise of Oxygen Molecules at Terapascal Pressures*, Phys. Rev. Lett. **108**, 2 (2012).
- [38] L. Zhu, Z. Wang, Y. Wang, G. Zou, H. K. Mao, and Y. Ma, *Spiral Chain O 4 Form of Dense Oxygen*, Proc. Natl. Acad. Sci. U. S. A. **109**, 751 (2012).
- [39] B. H. Cogollo-Olivo, S. Biswas, S. Scandolo, and J. A. Montoya, *Phase Diagram of Oxygen at Extreme Pressure and Temperature Conditions: An Ab Initio Study*, Phys. Rev. B **98**, 1 (2018).
- [40] S. F. Elatresh, V. Askarpour, and S. A. Bonev, $E-\zeta$ Transition in Solid Oxygen S., Phys.

- Rev. B **110**, 064106 (2024).
- [41] K. Takemura, S. Minomura, O. Shimomura, and Y. Fujii, *Observation of Molecular Dissociation of Iodine at High Pressure by X-Ray Diffraction*, Phys. Rev. Lett. **45**, 1881 (1980).
- [42] M. Pasternak, J. N. Farrell, and R. D. Taylor, *Metallization and Structural Transformation of Iodine under Pressure: A Microscopic View*, Phys. Rev. Lett. **58**, 575 (1987).
- [43] A. W. H. Olijinyk, W. Li, *High-Pressure Studies Of Solid Iodine by Raman Spectroscopy*, Phys. Rev. B **50**, 712 (1994).
- [44] N. Sakai, K. Takemura, and K. Tsuji, *Electrical Properties of High-Pressure Metallic Modification of Iodine*, J. Phys. Soc. Japan **51**, 1811 (1982).
- [45] C. Shimomura, K. Takemura, Y. Fujii, S. Minomura, M. Mori, Y. Noda, and Y. Yamada, *Structure Analysis of High-Pressure Metallic State of Iodine*, Phys. Rev. B **18**, 715 (1978).
- [46] P. Li, G. Gao, and Y. Ma, *Modulated Structure and Molecular Dissociation of Solid Chlorine at High Pressures*, J. Chem. Phys. **137**, (2012).
- [47] P. Dalladay-Simpson, J. Binns, M. Peña-Alvarez, M. E. Donnelly, E. Greenberg, V. Prakapenka, X. J. Chen, E. Gregoryanz, and R. T. Howie, *Band Gap Closure, Incommensurability and Molecular Dissociation of Dense Chlorine*, Nat. Commun. **10**, 1 (2019).
- [48] D. Duan, Z. Liu, Z. Lin, H. Song, H. Xie, T. Cui, C. J. Pickard, and M. Miao, *Multistep Dissociation of Fluorine Molecules under Extreme Compression*, Phys. Rev. Lett. **126**, 225704 (2021).
- [49] E. Bykova, I. G. Batyrev, M. Bykov, E. Edmund, S. Chariton, V. B. Prakapenka, and A. F. Goncharov, Structural Evolution of Iodine on Approach to the Monatomic State, Phys. Rev. B 108, 024104 (2023).
- [50] Y. Yin, A. Aslandukov, M. Bykov, D. Laniel, A. Aslandukova, A. Pakhomova, T. Fedotenko, W. Zhou, F. I. Akbar, M. Hanfland, K. Glazyrin, C. Giacobbe, E. L. Bright, G. Garbarino, Z. Jia, N. Dubrovinskaia, and L. Dubrovinsky, *Polytypism of Incommensurately Modulated Structures of Crystalline Bromine upon Molecular Dissociation under High Pressure*, Phys. Rev. B 110, 104111 (2024).
- [51] C. E. Weir, G. J. Piermarini, and S. Block, *Crystallography of Some High-Pressure Forms of C6H6, CS2, Br2, CCl4, and KNO3*, J. Chem. Phys. **50**, 2089 (1969).
- [52] Y. Fujii, K. Hase, Y. Ohishi, H. Fujihisa, N. Hamaya, K. Takemura, O. Shimomura, T.

- Kikegawa, Y. Amemiya, and T. Matsushita, *Evidence for Molecular Dissociation in Bromine near 80 GPa*, Phys. Rev. Lett. **63**, 536 (1989).
- [53] H. Fujihisa, Y. Fujii, K. Takemura, and O. Shimomura, Structural Aspects of Dense Solid Halogens under High Pressure Studied by X-Ray Diffraction—Molecular Dissociation and Metallization, J. Phys. Chem. Solids **56**, 1439 (1995).
- [54] Y. Akahama, H. Kawamura, H. Fujihisa, K. Aoki, and Y. Fujii, *Raman Spectra of Solid Bromine under Pressure of up to 80 GPa*, Rev. High Press. Sci. Technol. **7**, 793 (1998).
- [55] K. Yamaguchi and H. Miyagi, *First-Principles Study of Solid Iodine and Bromine under High Pressure*, J. Phys. Condens. Matter **10**, 11203 (1998).
- [56] S. Miao, E. Van Doren, and J. L. Martins, *Density-Functional Studies of High-Pressure Properties and Molecular Dissociations of Halogen Molecular Crystals*, Phys. Rev. B **68**, 1 (2003).
- [57] D. Duan, Y. Liu, Y. Ma, Z. Liu, T. Cui, B. Liu, and G. Zou, *Ab Initio Studies of Solid Bromine under High Pressure*, Phys. Rev. B Condens. Matter Mater. Phys. **76**, 1 (2007).
- [58] M. Wu, J. S. Tse, and Y. Pan, *Anomalous Bond Length Behavior and a New Solid Phase of Bromine under Pressure*, Sci. Rep. **6**, 1 (2016).
- [59] P. Li, X. Du, G. Gao, R. Sun, L. Zhang, and W. Wang, *New Modulated Structures of Solid Bromine at High Pressure*, Comput. Mater. Sci. **171**, 109205 (2020).
- [60] S. Zhao, J. Gao, Q.-J. Liu, D.-H. Fan, and Z.-T. Liu, *Pressure Dependence of Superconducting Behavior of Solid Br and I: A First-Principles Study*, Mater. Today Commun. **40**, 109939 (2024).
- [61] M. Rahm, T. Zeng, and R. Hoffmann, *Electronegativity Seen as the Ground-State Average Valence Electron Binding Energy*, J. Am. Chem. Soc. **141**, 342 (2019).
- [62] M. A. Olson, S. Bhatia, P. Larson, and B. Militzer, *Prediction of Chlorine and Fluorine Crystal Structures at High Pressure Using Symmetry Driven Structure Search with Geometric Constraints*, J. Chem. Phys. **153**, (2020).
- [63] X. Dong, A. R. Oganov, H. Cui, X.-F. Zhou, and H.-T. Wang, *Electronegativity and Chemical Hardness of Elements under Pressure*, Proc. Natl. Acad. Sci. **119**, 1 (2022).
- [64] M. Rahm, R. Cammi, N. W. Ashcroft, and R. Hoffmann, Squeezing All Elements in the Periodic Table: Electron Configuration and Electronegativity of the Atoms under Compression, J. Am. Chem. Soc. 141, 10253 (2019).
- [65] K. S. Thanthiriwatte, M. Vasiliu, D. a Dixon, and K. O. Christe, Structural and Energetic Properties of Closed Shell XF n (X = Cl, Br, and I; n = 1-7) and XO n F m

- (X = Cl, Br, and I; n = 1-3; m = 0-6) Molecules and Ions Leading to Stability Predictions for Yet Unknown Compounds, Inorg. Chem. **51**, 10966 (2012).
- [66] R. D. Burbank and F. N. Bensey, *The Structures of the Interhalogen Compounds.* * *I. Chlorine Trifluoride at 120°C*, J. Chem. Phys. **21**, 602 (1953).
- [67] R. D. Burbank and F. N. Bensey, Structure of the Interhalogen Compounds. III. Concluding Note on Bromide Trifluoride, Bromine Pentafluoride, and Iodine Pentafluoride, J. Chem. Phys. 27, 982 (1957).
- [68] R. D. Burbank and F. N. Bensey, *Structure of the Interhalogen Compounds. II. Iodine Heptafluoride at -110°C and at -145°C*, J. Chem. Phys. **27**, 904 (1957).
- [69] D. W. Magnuson, *Microwave Spectrum and Molecular Structure of Bromine Trifluoride*, J. Chem. Phys. **27**, 223 (1957).
- [70] R. Boese, A. Daniel Boese, D. Bläser, M. Y. Antipin, A. Ellern, and K. Seppelt, *The Surprising Crystal Packing of Chlorinefluoride*, Angew. Chemie (International Ed. English) **36**, 1489 (1997).
- [71] R. D. Durbank and G. R. Jones, *Crystal Structure of Iodine Pentafluoride at -80.Deg.*, Inorg. Chem. **13**, 1071 (1974).
- [72] D. Luo, J. Lv, F. Peng, Y. Wang, G. Yang, M. Rahm, and Y. Ma, *A Hypervalent and Cubically Coordinated Molecular Phase of IF 8 Predicted at High Pressure*, Chem. Sci. **10**, 2543 (2019).
- [73] M. Möbs, T. Graubner, K. Eklund, A. J. Karttunen, and F. Kraus, *Bromine Pentafluoride* BrF 5, the Formation of [BrF 6] Salts, and the Stereochemical (In)Activity of the Bromine Lone Pairs, Chem. A Eur. J. 28, e202202466 (2022).
- [74] A. L. Ruoff, Stress Anisotropy in Opposed Anvil High-pressure Cells, J. Appl. Phys. **46**, 1389 (1975).
- [75] S. Klotz, J. C. Chervin, P. Munsch, and G. Le Marchand, *Hydrostatic Limits of 11 Pressure Transmitting Media*, J. Phys. D. Appl. Phys. **42**, (2009).
- [76] A. Celeste, F. Borondics, and F. Capitani, *Hydrostaticity of Pressure-Transmitting Media for High Pressure Infrared Spectroscopy*, High Press. Res. **39**, 608 (2019).
- [77] B. L. Brugman, M. Lv, J. Liu, E. Greenberg, V. B. Prakapenka, D. Y. Popov, C. Park, and S. M. Dorfman, *Strength, Deformation, and the Fcc-Hcp Phase Transition in Condensed Kr and Xe to the 100 GPa Pressure Range*, J. Appl. Phys. **137**, (2025).
- [78] E. Schrödinger, *An Undulatory Theory of the Mechanics of Atoms and Molecules*, Phys. Rev. **28**, 1049 (1926).
- [79] D. S. Sholl and J. A. Steckel, *Density Functional Theory* (Wiley, 2009).

- [80] M. Born and R. Oppenheimer, *Zur Quantentheorie Der Molekeln*, Ann. Phys. **389**, 457 (1927).
- [81] D. R. Hartree, *The Wave Mechanics of an Atom with a Non-Coulomb Central Field.*Part I. Theory and Methods, Math. Proc. Cambridge Philos. Soc. **24**, 89 (1928).
- [82] D. R. Hartree, *The Wave Mechanics of an Atom with a Non-Coulomb Central Field.*Part II. Some Results and Discussion, Math. Proc. Cambridge Philos. Soc. 24, 111 (1928).
- [83] D. R. Hartree, *The Wave Mechanics of an Atom with a Non-Coulomb Central Field.*Part III. Term Values and Intensities in Series in Optical Spectra, Math. Proc. Cambridge Philos. Soc. **24**, 426 (1928).
- [84] D. R. Hartree, *The Wave Mechanics of an Atom with a Non-Coulomb Central Field.*Part IV. Further Results Relating to Terms of the Optical Spectrum, Math. Proc. Cambridge Philos. Soc. 25, 310 (1929).
- [85] Douglas Rayner Hartree and W. Hartree, *Self-Consistent Field*, *with Exchange*, *for Beryllium*, Proc. R. Soc. London. Ser. A Math. Phys. Sci. **150**, 9 (1935).
- [86] J. C. Slater, The Self Consistent Field and the Structure of Atoms, Phys. Rev. **32**, 339 (1928).
- [87] J. C. Slater, *Note on Hartree's Method*, Phys. Rev. **35**, 210 (1930).
- [88] J. C. Slater, Atomic Shielding Constants, Phys. Rev. 36, 57 (1930).
- [89] L. H. Thomas, *The Calculation of Atomic Fields*, Math. Proc. Cambridge Philos. Soc. 23, 542 (1927).
- [90] E. Fermi, A Statistical Method for Determining Some Properties of the Atom., Rend. Accad. Naz. Lincei 6, 602 (1927).
- [91] P. Hohenberg and W. Kohn, *Inhomogeneous Electron Gas*, Phys. Rev. **136**, B864 (1964).
- [92] W. Kohn and L. J. Sham, *Self-Consistent Equations Including Exchange and Correlation Effects*, Phys. Rev. **140**, A1133 (1965).
- [93] W. Kohn, *Nobel Lecture: Electronic Structure of Matter—Wave Functions and Density Functionals*, Rev. Mod. Phys. **71**, 1253 (1999).
- [94] J. P. P. and K. Schmidt, *Jacob's Ladder of Density Functional Approximations for the Exchange-Correlation Energy*, in *AIP Conference Proceedings*, Vol. 577 (AIP, 2001), pp. 1–20.
- [95] M. C. Payne, M. P. Teter, D. C. Allan, T. A. Arias, and J. D. Joannopoulos, *Iterative Minimization Techniques for Ab Initio Total-Energy Calculations: Molecular Dynamics*

- and Conjugate Gradients, Rev. Mod. Phys. 64, 1045 (1992).
- [96] P. Bagno, O. Jepsen, and O. Gunnarsson, *Ground-State Properties of Third-Row Elements with Nonlocal Density Functionals*, Phys. Rev. B **40**, 1997 (1989).
- [97] F. Herman, J. P. Van Dyke, and I. B. Ortenburger, *Improved Statistical Exchange Approximation for Inhomogeneous Many-Electron Systems*, Phys. Rev. Lett. **22**, 807 (1969).
- [98] J. P. Perdew and Y. Wang, *Accurate and Simple Analytic Representation of the Electron-Gas Correlation Energy*, Phys. Rev. B **45**, 13244 (1992).
- [99] J. P. Perdew, J. A. Chevary, S. H. Vosko, K. A. Jackson, M. R. Pederson, D. J. Singh, and C. Fiolhais, *Atoms, Molecules, Solids, and Surfaces: Applications of the Generalized Gradient Approximation for Exchange and Correlation*, Phys. Rev. B **46**, 6671 (1992).
- [100] J. P. Perdew, K. Burke, and M. Ernzerhof, *Generalized Gradient Approximation Made Simple*, Phys. Rev. Lett. **77**, 3865 (1996).
- [101] J. P. Perdew, S. Kurth, A. Zupan, and P. Blaha, *Accurate Density Functional with Correct Formal Properties: A Step Beyond the Generalized Gradient Approximation*, Phys. Rev. Lett. **82**, 2544 (1999).
- [102] J. Tao, J. P. Perdew, V. N. Staroverov, and G. E. Scuseria, *Climbing the Density Functional Ladder: Nonempirical Meta–Generalized Gradient Approximation Designed for Molecules and Solids*, Phys. Rev. Lett. **91**, 3 (2003).
- [103] Y. Zhao and D. G. Truhlar, A New Local Density Functional for Main-Group Thermochemistry, Transition Metal Bonding, Thermochemical Kinetics, and Noncovalent Interactions, J. Chem. Phys. 125, (2006).
- [104] J. Sun, A. Ruzsinszky, and J. Perdew, *Strongly Constrained and Appropriately Normed Semilocal Density Functional*, Phys. Rev. Lett. **115**, 036402 (2015).
- [105] A. P. Bartók and J. R. Yates, Regularized SCAN Functional, J. Chem. Phys. 150, (2019).
- [106] J. W. Furness, A. D. Kaplan, J. Ning, J. P. Perdew, and J. Sun, *Accurate and Numerically Efficient r 2 SCAN Meta-Generalized Gradient Approximation*, J. Phys. Chem. Lett. **11**, 8208 (2020).
- [107] A. D. Becke, A New Mixing of Hartree–Fock and Local Density-Functional Theories, J. Chem. Phys. **98**, 1372 (1993).
- [108] J. Heyd, G. E. Scuseria, and M. Ernzerhof, *Hybrid Functionals Based on a Screened Coulomb Potential*, J. Chem. Phys. **118**, 8207 (2003).
- [109] M. Liu, A. Gopakumar, V. I. Hegde, J. He, and C. Wolverton, *High-Throughput Hybrid-Functional DFT Calculations of Bandgaps and Formation Energies and Multifidelity*

- Learning with Uncertainty Quantification, Phys. Rev. Mater. 8, 043803 (2024).
- [110] D. R. Hamann, M. Schlüter, and C. Chiang, *Norm-Conserving Pseudopotentials*, Phys. Rev. Lett. **43**, 1494 (1979).
- [111] D. Vanderbilt, Soft Self-Consistent Pseudopotentials in a Generalized Eigenvalue Formalism, Phys. Rev. B 41, 7892 (1990).
- [112] G. Kresse and D. Joubert, From Ultrasoft Pseudopotentials to the Projector Augmented-Wave Method, Phys. Rev. B **59**, 1758 (1999).
- [113] P. E. Blöchl, Projector Augmented-Wave Method, Phys. Rev. B 50, 17953 (1994).
- [114] S. Grimme, Accurate Description of van Der Waals Complexes by Density Functional Theory Including Empirical Corrections, J. Comput. Chem. **25**, 1463 (2004).
- [115] S. Grimme, Semiempirical GGA-type Density Functional Constructed with a Long-range Dispersion Correction, J. Comput. Chem. 27, 1787 (2006).
- [116] S. Grimme, J. Antony, S. Ehrlich, and H. Krieg, A Consistent and Accurate Ab Initio Parametrization of Density Functional Dispersion Correction (DFT-D) for the 94 Elements H-Pu, J. Chem. Phys. 132, (2010).
- [117] J. Moellmann and S. Grimme, *DFT-D3 Study of Some Molecular Crystals*, J. Phys. Chem. C **118**, 7615 (2014).
- [118] S. Ehlert, U. Huniar, J. Ning, J. W. Furness, J. Sun, A. D. Kaplan, J. P. Perdew, and J. G. Brandenburg, R 2 SCAN-D4: Dispersion Corrected Meta-Generalized Gradient Approximation for General Chemical Applications, J. Chem. Phys. 154, 061101 (2021).
- [119] P. C. Müller, C. Ertural, J. Hempelmann, and R. Dronskowski, *Crystal Orbital Bond Index: Covalent Bond Orders in Solids*, J. Phys. Chem. C **125**, 7959 (2021).
- [120] C. Ertural, S. Steinberg, and R. Dronskowski, *Development of a Robust Tool to Extract Mulliken and Löwdin Charges from Plane Waves and Its Application to Solid-State Materials*, RSC Adv. **9**, 29821 (2019).
- [121] D. C. Lonie and E. Zurek, *XtalOpt: An Open-Source Evolutionary Algorithm for Crystal Structure Prediction*, Comput. Phys. Commun. **182**, 372 (2011).
- [122] G. Kresse and J. Furthmüller, *Efficient Iterative Schemes for Ab Initio Total-Energy Calculations Using a Plane-Wave Basis Set*, Phys. Rev. B **54**, 11169 (1996).
- [123] P. Giannozzi, S. Baroni, N. Bonini, M. Calandra, R. Car, C. Cavazzoni, D. Ceresoli, G. L. Chiarotti, M. Cococcioni, I. Dabo, A. Dal Corso, S. de Gironcoli, S. Fabris, G. Fratesi, R. Gebauer, U. Gerstmann, C. Gougoussis, A. Kokalj, M. Lazzeri, L. Martin-Samos, N. Marzari, F. Mauri, R. Mazzarello, S. Paolini, A. Pasquarello, L. Paulatto, C. Sbraccia, S. Scandolo, G. Sclauzero, A. P. Seitsonen, A. Smogunov, P. Umari, and R. M.

- Wentzcovitch, *QUANTUM ESPRESSO: A Modular and Open-Source Software Project for Quantum Simulations of Materials*, J. Phys. Condens. Matter **21**, 395502 (2009).
- [124] J. D. Gale, Empirical Potential Derivation for Ionic Materials, Philos. Mag. B 73, 3 (1996).
- [125] J. D. Gale, GULP: A Computer Program for the Symmetry-Adapted Simulation of Solids, J. Chem. Soc. Faraday Trans. 93, 629 (1997).
- [126] J. D. Gale and A. L. Rohl, *The General Utility Lattice Program (GULP)*, Mol. Simul. **29**, 291 (2003).
- [127] S. M. Woodley, Engineering Microporous Architectures: Combining Evolutionary Algorithms with Predefined Exclusion Zones, Phys. Chem. Chem. Phys. 9, 1070 (2007).
- [128] D. M. Deaven and K. M. Ho, *Molecular Geometry Optimization with a Genetic Algorithm*, Phys. Rev. Lett. **75**, 288 (1995).
- [129] B. Hartke, Global Cluster Geometry Optimization by a Phenotype Algorithm with Niches: Location of Elusive Minima, and Low-Order Scaling with Cluster Size, J. Comput. Chem. **20**, 1752 (1999).
- [130] B. Bandow and B. Hartke, Larger Water Clusters with Edges and Corners on Their Way to Ice: Structural Trends Elucidated with an Improved Parallel Evolutionary Algorithm, J. Phys. Chem. A 110, 5809 (2006).
- [131] B. Assadollahzadeh, P. R. Bunker, and P. Schwerdtfeger, *The Low Lying Isomers of the Copper Nonamer Cluster, Cu9*, Chem. Phys. Lett. **451**, 262 (2008).
- [132] B. Assadollahzadeh and P. Schwerdtfeger, *A Systematic Search for Minimum Structures of Small Gold Clusters Aun* (*N*=2–20) and Their Electronic Properties, J. Chem. Phys. **131**, (2009).
- [133] N. L. Abraham and M. I. J. Probert, A Periodic Genetic Algorithm with Real-Space Representation for Crystal Structure and Polymorph Prediction, Phys. Rev. B 73, 224104 (2006).
- [134] G. Trimarchi and A. Zunger, *Global Space-Group Optimization Problem: Finding the Stablest Crystal Structure without Constraints*, Phys. Rev. B **75**, 104113 (2007).
- [135] J. Hooper, A. Hu, F. Zhang, and T. K. Woo, Genetic Algorithm and First-Principles DFT Study of the High-Pressure Molecular ζ Phase of Nitrogen, Phys. Rev. B 80, 104117 (2009).
- [136] A. R. Oganov and C. W. Glass, *Crystal Structure Prediction Using Ab Initio Evolutionary Techniques: Principles and Applications*, J. Chem. Phys. **124**, (2006).
- [137] C. W. Glass, A. R. Oganov, and N. Hansen, USPEX—Evolutionary Crystal Structure

- Prediction, Comput. Phys. Commun. 175, 713 (2006).
- [138] Z. Falls, P. Avery, X. Wang, K. P. Hilleke, and E. Zurek, *The XtalOpt Evolutionary Algorithm for Crystal Structure Prediction*, J. Phys. Chem. C **125**, 1601 (2021).
- [139] X. Ye, N. Zarifi, E. Zurek, R. Hoffmann, and N. W. Ashcroft, *High Hydrides of Scandium under Pressure: Potential Superconductors*, J. Phys. Chem. C **122**, 6298 (2018).
- [140] W. Cui, T. Bi, J. Shi, Y. Li, H. Liu, E. Zurek, and R. J. Hemley, *Route to High-Tc Superconductivity via CH4-Intercalated H3S Hydride Perovskites*, Phys. Rev. B **101**, 134504 (2020).
- [141] K. P. Hilleke, X. Wang, D. Luo, N. Geng, B. Wang, F. Belli, and E. Zurek, *Structure, Stability, and Superconductivity of N-Doped Lutetium Hydrides at Kbar Pressures*, Phys. Rev. B **108**, 014511 (2023).
- [142] S. Baroni, P. Giannozzi, and E. Isaev, *Density-Functional Perturbation Theory for Ouasi-Harmonic Calculations*, Rev. Mineral. Geochemistry **71**, 39 (2010).
- [143] M. T. Dove and C. A. Condat, *Introduction to Lattice Dynamics*, Am. J. Phys. **62**, 1051 (1994).
- [144] G. P. Srivastava, The Physics of Phonons (CRC Press, Boca Raton, 2022).
- [145] A. Togo and I. Tanaka, First Principles Phonon Calculations in Materials Science, Scr. Mater. 108, 1 (2015).
- [146] K. Parlinski, Lattice Dynamics: Vibrational Modes, in Encyclopedia of Condensed Matter Physics (Elsevier, 2005), pp. 98–102.
- [147] P. Giannozzi, S. de Gironcoli, P. Pavone, and S. Baroni, *Ab Initio Calculation of Phonon Dispersions in Semiconductors*, Phys. Rev. B **43**, 7231 (1991).
- [148] X. Gonze and C. Lee, Dynamical Matrices, Born Effective Charges, Dielectric Permittivity Tensors, and Interatomic Force Constants from Density-Functional Perturbation Theory, Phys. Rev. B 55, 10355 (1997).
- [149] S. Baroni, S. de Gironcoli, A. Dal Corso, and P. Giannozzi, *Phonons and Related Crystal Properties from Density-Functional Perturbation Theory*, Rev. Mod. Phys. **73**, 515 (2001).
- [150] A. Togo, L. Chaput, I. Tanaka, and G. Hug, First-Principles Phonon Calculations of Thermal Expansion in Ti3SiC2, Ti3AlC2, and Ti3GeC2, Phys. Rev. B **81**, 174301 (2010).
- [151] D. Porezag and M. R. Pederson, *Infrared Intensities and Raman-Scattering Activities within Density-Functional Theory*, Phys. Rev. B **54**, 7830 (1996).

- [152] J. M. Skelton, L. A. Burton, A. J. Jackson, F. Oba, S. C. Parker, and A. Walsh, *Lattice Dynamics of the Tin Sulphides SnS 2*, *SnS and Sn 2 S 3*: *Vibrational Spectra and Thermal Transport*, Phys. Chem. Chem. Phys. **19**, 12452 (2017).
- [153] M. Levy, 1. Introduction to Fundamentals of Elastic Constants, in Experimental Methods in the Physical Sciences, Vol. 39 (2001), pp. 1–35.
- [154] M. Born and K. Huang, *Quantum Mechanical Foundation*, in *Dynamical Theory Of Crystal Lattices* (Oxford University PressNew York, NY, 1996), pp. 166–212.
- [155] F. Mouhat and F.-X. Coudert, *Necessary and Sufficient Elastic Stability Conditions in Various Crystal Systems*, Phys. Rev. B **90**, 224104 (2014).
- [156] A. San-Miguel, H. Libotte, M. Gauthier, G. Aquilanti, S. Pascarelli, and J. P. Gaspard, New Phase Transition of Solid Bromine under High Pressure, Phys. Rev. Lett. **99**, 1 (2007).
- [157] B. M. Powell, K. M. Heal, and B. H. Torrie, *The Temperature Dependence of the Crystal Structures of the Solid Halogens, Bromine and Chlorine*, Mol. Phys. **53**, 929 (1984).
- [158] M. W. Chase, NIST-JANAF Thermochemical Tables, 4th Ed. J. Phys. Chem. Ref. Data. 1998, Monograph 9(Part I and Part II), Journal of Physical and Chemical Reference Data.
- [159] P. G. Johannsen, W. Helle, and W. B. Holzapfel, *Effect of Pressure on Raman Spectra of Solid Bromine*, High Press. Res. **3**, 227 (1990).
- [160] T. Kume, T. Hiraoka, Y. Ohya, S. Sasaki, and H. Shimizu, *High Pressure Raman Study of Bromine and Iodine: Soft Phonon in the Incommensurate Phase*, Phys. Rev. Lett. **94**, 1 (2005).
- [161] Y. Fujii, K. Hase, N. Hamaya, Y. Ohishi, A. Onodera, O. Shimomura, and K. Takemura, Pressure-Induced Face-Centered-Cubic Phase of Monatomic Metallic Iodine, Phys. Rev. Lett. 58, 796 (1987).